UNDERSTANDING THE WESTERN WADDEN SEA IN TERMS OF INLET CONNECTIVITY: AN EXPLORATORY MODELLING APPROACH

A THESIS SUBMITTED FOR THE DEGREE OF MASTER OF SCIENCE IN CIVIL ENGINEERING AND MANAGEMENT.

WOUT PLOEG

UNDER SUPERVISION OF

Dr. Ir. P.C. ROOS
Dr. Ir. T.M. DUONG
Prof. Dr. H.M. SCHUTTELAARS

FINAL DRAFT, FEBRUARY 16, 2023

UNIVERSITY OF TWENTE.

"Als je heel diep over iets nadenkt, kom je vanzelf uit bij iets dat niet klopt. Probeer maar eens - klopt altijd!"

Herman Finkers

Acknowledgements

Abstract

Barrier coasts are characterised by a chain of barrier islands, separated by tidal inlets that connect the outer sea to the basin. Improving our understanding of these is crucial in managing these areas, which are often subject to conflicting interests between ecology, economy and coastal safety. This study focuses on cross-sectional stability (whether the system returns to equilibrium after a perturbation) and connectivity (to which extent perturbations at one inlet lead to cross-sectional changes of other inlets) of double and triple inlet systems. For this purpose, an idealised process-based model based in the Escoffier (1940) principle is developed, that allows for basins with plan view shape like the sector of a circle and for a tidal divide to be present along a constant radial coordinate. It is investigated how tidal inlet stability and connectivity are influenced by 1) changing to this sectoral basin geometry; 2) changing from a double to a triple inlet system; 3) including a tidal divide circumventing the middle inlet. The results, obtained for symmetric systems, indicate that the basin area is a key factor in inlet stability and connectivity and that including such a tidal divide reduces the connectivity between all inlets. Furthermore, a direct correlation between asymmetry in the cross-sectional area of the inlets and asymmetry in the inlet connectivity is found, independent of the presence of the tidal divide but dependent on the basin area, resulting from the competition between the bottom friction in and pressure-gradient over the inlets.

Keywords: Barrier coast, tidal inlet stability, connectivity, tidal divide.

Samenvatting

Barrière kusten worden gekenmerkt door een rij van barrière eilanden, gescheiden door zeegaten die de zee verbinden met de binnenzee. Voor het succesvol beheren van dit soort gebieden is fundamenteel begrip van deze gebieden van essentieel belang, aangezien dit soort gebieden vaak onderhevig zijn aan verschillende belangen op het gebied van ecologie, economie en kustonderhoud. Deze studie focust op de stabiliteit van de dwarsdoorsnede (of het systeem terugkeert naar equilibrium als het verstoord wordt) en connectiviteit (in hoeverre een verstoring van één zeegat leidt tot grootte-veranderingen van de andere zeegaten) in systemen met twee en drie zeegaten. Daartoe is een geïdealiseerd model ontwikkeld, gebasseerd op het principe van Escoffier (1940), waarin binnenzeeën met een bovenaanzicht als een sector van een cirkel gemodelleerd worden en waarin een wantij langs een constante radiale coordinaat kan worden aangebracht. Hiermee wordt onderzocht hoe de stabiliteit en connectiviteit van de zeegaten beïnvloed wordt door 1) het modelleren van de binnenzee als een sector van een cirkel; 2) het uitbreiden van het systeem van twee naar drie zeegaten; 3) en het meenemen van een wantij rondom het middelste zeegat. De resultaten voor symmetrische systemen laten zien dat de oppervlakte van de binnenzee van groot belang is op de stabiliteit en connectiviteit en dat het meenemen van het wantij leidt tot een lagere connectiviteit tussen alle zeegaten. Daarnaast is er een directe correlatie gevonden tussen asymmetrie in de oppervlakte van de zeegaten en de asymmetrie in de connectiviteit. Dit is onafhankelijk van de aanwezigheid van het wantij en het gevolg van de bodemfrictie in en het drukverschil over de zeegaten.

Contents

1 Introduction

WORLDWIDE, roughly 40 per cent of the world population lives close to the coast. Furthermore, 10 to 15% of the worldwide coastline is classified as a so-called barrier coast (De Swart & Zimmerman, 2009). As this type of coast is generally used for many different activities, ranging from fishery and navigation to wildlife excursions, these areas can be subject to conflicting interests between ecology, economy and coastal safety (Brouwer et al., 2013). Furthermore, research has shown that local interventions can result in large-scale changes in these areas (e.g. Reef et al., 2020), yielding the need for a detailed understanding of the dynamics in barrier coasts. Key questions to answer are, for instance, whether a barrier coast will persist in its current shape on large timescales and to what extent small local perturbations lead to changes elsewhere in the system.

A barrier coast (see Figure 1a for an example) is characterised by the presence of one or more barrier island(s), separating the sea from a back-barrier basin. The basin and sea are connected by one or more tidal inlets, allowing the tidal motion to propagate into the basin (De Swart & Zimmerman, 2009). Due to wind waves and tidal currents, a sediment flow (littoral drift) along the seaward shore of the barrier islands exists. Upon reaching the inlets, part of this sediment will be transported into the inlet by the tidal current, allowing sedimentation of the inlet to occur (De Swart & Zimmerman, 2009). Contrastingly, strong inlet flow can lead to inlet erosion, adding sediment to the long-shore transport. As such, the tidal flow through the inlets can lead to morphodynamic development of the inlets, which, in turn, can influence the inlet flows via depth-dependent bottom friction and a smaller cross-sectional inlet area available to transport the tidal prism. Hence, a strong feedback is potentially present in the system.

In this study, we specifically focus on the Western Wadden Sea (the Netherlands), one of the world's most prominent mesotidal barrier coasts and acknowledged as UNESCO World Heritage due to its ecological value (UNESCO World Heritage Centre, 2009). In Figure 1a, a satellite view of this area is given, showing that the system consists of three inlets, with a tidal divide (white lines) separating the middle inlet (Eierlandse Gat) from the other two inlets (the Texel and Vlie inlets). Another tidal divide separates the basin between the Texel and Vlie inlets.

One of the key properties of the behaviour of a barrier coast is whether one or multiple inlets will close on a morphodynamic timescale (order of decades to centuries), as it is known that tidal inlets can close as a result of sedimentation (De Swart & Zimmerman, 2009). Mathematically, this can be quantified by the concept of the cross-sectional stability of tidal inlets following the principle of Escoffier (1940). This principle is graphically illustrated in Figure 2a, where the inlet flow velocity amplitude is plotted against the cross-sectional inlet area. An equilibrium state (denoted with A and B in the figure) is reached in case the velocity amplitude equals the equilibrium velocity ampli-
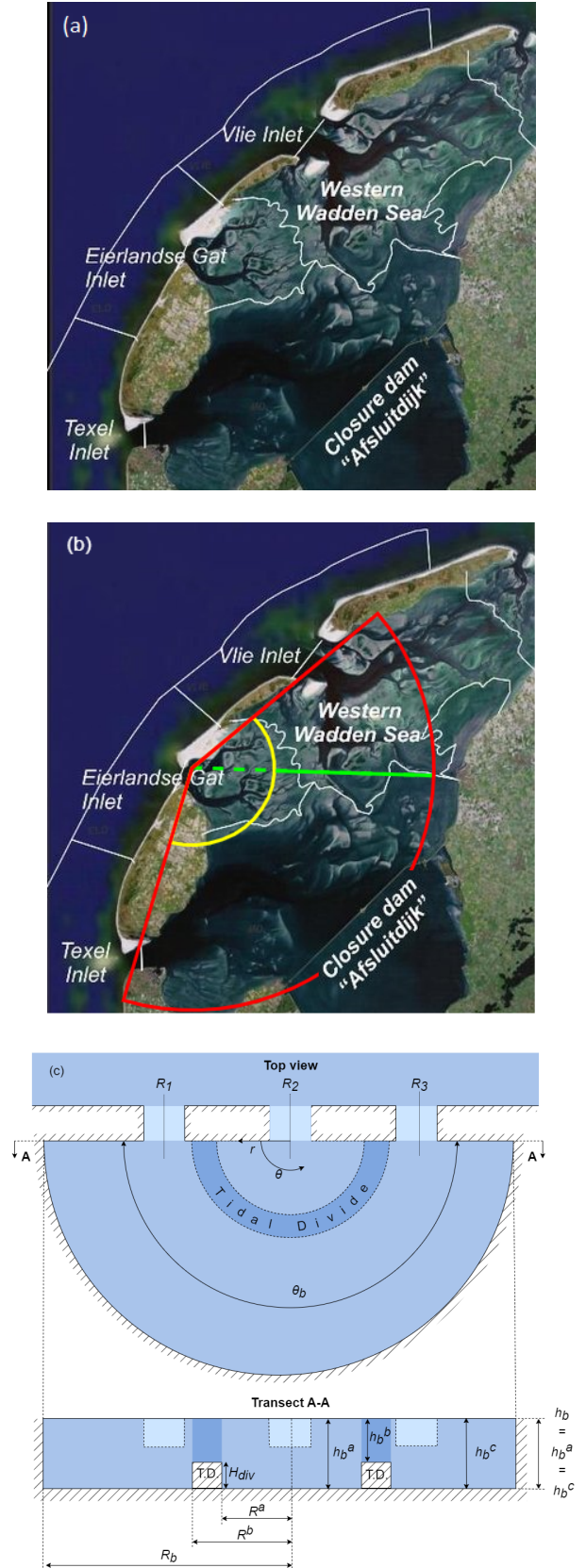

Figure 1: (a) Satellite image of the Western Wadden Sea with tidal divides in white, courtesy to Elias et al. (2012). (b) Impression of the schematisation of the Western Wadden Sea in this study (Elias et al., 2012, adapted). (c) Definition sketch of the schematic system with dashed tidal divides for $\theta_b = 180°$.
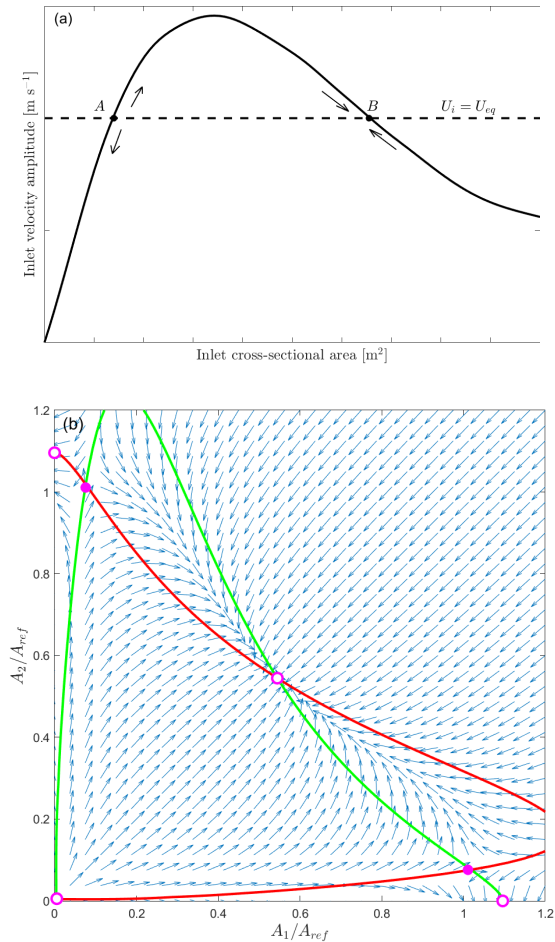
Figure 2: Visualisation of the Escoffier (1940) closure curve to assess tidal inlet stability in a single inlet system (top), and the flow-charts for assessing double inlet stability (bottom). In the latter, plotted are $dA_1/dt = 0$ (green), $dA_2/dt = 0$ (red), and stable (pink circles) and unstable (pink dots) equilibria.

tude: at both points, the cross-sectional area of the inlet will not change. However, these two equilibria respond differently to a perturbation of the cross-sectional area, as denoted by the arrows in Figure 2a. Equilibrium B is called stable, as it, "after having been perturbed, will return to that equilibrium." (van de Kreeke et al., 2008). On the contrary, equilibrium A is called unstable, as the inlet will not return to this equilibrium upon perturbation: when reducing its size, the inlet flow velocity reduces, yielding sedimentation and a further reduction of the inlet size until it has closed; conversely, increasing its size leads an increase in the flow velocity, yielding erosion and a further increase of the inlet area, until equilibrium B has been reached. This concept is relatively easily expanded to a multiple inlet system by applying the Escoffier principle to each inlet individually, yielding flowcharts with one axis for the cross-sectional area of each inlet. The vectors then show how the area of each inlet will change for a given combination of inlet areas (see Figure 2b).

Multiple authors have already investigated tidal inlet stability, for instance with empirical data (see e.g.

Kragtwijk et al., 2004; Stive et al., 1998), detailed numerical models for hydrodynamics and morphology (e.g. Salles et al., 2005) and exploratory modelling approaches (e.g. Roos et al., 2013; van de Kreeke et al., 2008). Each of these methods has its advantages and disadvantages, but this study aims to acquire a fundamental, system-level understanding of a triple inlet system with a tidal divide separating the middle inlet from the outer two. For such an objective, exploratory modelling approaches are best suited as these only include the most essential processes and leave out site-specific details (Murray, 2003). Hence, such models can be applied with low-computational demand and allow for distinct investigation of the effect of various processes on the results.

Using such an exploratory model, Roos et al. (2013) have shown that including water level variations in the basin is sufficient to simulate stable equilibrium configurations with multiple open inlets. Multiple authors have further expanded this model, showing that water level variations in the ocean (realised by including radiative damping) can also lead to stable equilibria (Brouwer et al., 2013). Others investigated the influence of inlet entrance and exit losses (Brouwer et al., 2012) and basin geometry (Reef et al., 2020). In Roos & Schuttelaars (to be published) and van de Kreeke et al. (2008), the presence of a tidal divide is also investigated, but both models do not allow for separating the middle inlet from the outer two. As the basin in both studies is chosen as a rectangular basin with the tidal divides perpendicular to the coast, introducing a divide over the complete (cross-shore) basin width between inlets one and two would also affect the exchange between inlets one and three. Furthermore, the entire solution method collapses in case one decides to place the divides as a box around the middle inlet. The model by Reef et al. (2020) leaves some more freedom in the choice of the basin shape but does not accommodate the presence of tidal divides in the system. Furthermore, this method is depending to a relatively large degree on numerical solving, which is not preferable if one manages to find a model formulation that is to a larger degree analytically solvable. Additionally, in the current modelling studies (see e.g. Roos et al., 2013; van de Kreeke, 1990; van de Kreeke et al., 2008, Roos & Schuttelaars, to be published), the Western Wadden Sea system was always modelled as a double inlet system consisting of the Texel and Vlie inlets. The Eierlandse Gat was omitted as a result of the low water exchange over the present tidal divide (Zimmerman, 1976). Hence, the effect of a tidal divide has only been studied for the same double inlet system (Roos & Schuttelaars, to be published).

This study, therefore, aims to investigate the behaviour of the Western Wadden Sea more thoroughly by developing a model that contains three inlets and a circular tidal divide in the basin, employing the solution method by Roos et al. (2013) and Roos & Schuttelaars (to be published) but applied to a geometry with a sector-shaped basin, as shown in Figure 1b (red lines). This choice still allows for a similar solution procedure as applied in a.o. Roos et al. (2013), but does accommodate for isolation of the middle inlet by introducing a tidal divide

along a constant radial coordinate (Fig. 1b, yellow line). Introducing an axial tidal divide (Fig. 1b, solid green line) would, however, be more problematic as it would no longer allow for an analytical solution method. As the solution method is based on the separation of variables, the axial divide can only be included if it can be described independently of the radial coordinate. Hence, it must stretch from the origin to the boundary of the basin (Fig. 1b, solid and dashed green line), which is unrealistic and would introduce a very shallow area where the two divides intersect. Hence, this tidal divide is omitted in this study to enable an analytical mathematical solution technique, allowing for a thorough investigation of the system properties within the available computational power.

Furthermore, the concept of cross-sectional stability is not satisfactory in describing the system's behaviour after a perturbation at an inlet. After all, it only describes whether the system will return to equilibrium, but to what extent an intervention at one inlet will influence the morphodynamics at the other inlets remains unclear. To this end, Roos & Schuttelaars (to be published) introduced the connectivity quotient, a measure of "the extent to which changes in the geometry of one inlet lead to changes in the geometry of another inlet." (Roos & Schuttelaars, to be published). Not only does this concept yield more insight into the behaviour of the system, but it also allows for quantifying the effect of a tidal divide: as a tidal divide hinders the exchange of water between inlets, one would expect this to be reflected in the connectivity quotient as well.

The innovation in this paper is threefold: first, the known modelling technique by Roos et al. (2013) is reformulated for a circular-sector-shaped basin geometry. Secondly, the analysis is extended from a double to a triple inlet system. Thirdly, the basin geometry enables the presence of a radial tidal divide. For all three steps, this study aims to investigate the tidal inlet stability and connectivity properties of the system.

This report is organised as follows: in Section 2, the model is formulated for a sector-shaped basin geometry with a tidal divide. The solution strategy and analysis methods employed are described in resp. Sections 3 and 4. In Section 5, the solutions are presented, followed by the discussion (Sec. 6) and the conclusions (Sec. 7).

2 Model Formulation

2.1 Geometry of System

For this study, we consider a strongly schematised triple inlet system, consisting of a tidally forced ocean domain and a sector-shaped basin, connected by three inlets (see Figure 1c). In the basin, we introduce polar coordinates r and θ, such that $0 \leq r \leq R_b$ with R_b the radius of the basin, and $0 \leq \theta \leq \theta_b$ with θ_b the angle of the basin. The vertical coordinate z is introduced, defined such that $z = \eta$ equals the free surface elevation with zero spatial average, and $z = -h_b$ is the topography. Within the domain, two radial topographic steps are present, such that the bottom

depth h_b with respect to the horizontal datum is given by

$$h_b(r) = \begin{cases} h_b^a & \text{for } 0 < r < R^a, \\ h_b^b & \text{for } R^a < r < R^b, \\ h_b^c & \text{for } R^b < r < R_b, \end{cases} \quad (1)$$

where R^a, R^b denote the radial coordinates of the topographic steps, and superscripts a, b, c are used to denote the three different compartments of the basin. Consequently, the topography is uniform in each compartment, and the height of the tidal divide is given by $H_{div} = h_b^a - h_b^b = h_b^c - h_b^b$.

The inlets are centered around radial inlet coordinate $r = R_j$ on the boundaries $\theta_j = 0$ or $\theta_j = \theta_b$, and have a rectangular cross-section of width b_j and height h_j and length l. We require that the inlet positions do not overlap with each other, nor with one of the tidal steps in the domain, nor may the inlet exceed the radius of the basin. Generally, the inlet may also not continue over the origin; this is only allowed if $\theta_b = \pi$. In line with Roos et al. (2013), it is assumed that the depth-to-width ratio of each inlet is constant, i.e.

$$\gamma^2 = \frac{h_j}{b_j}, \qquad (h_j, b_j) = (\gamma, \gamma^{-1})\sqrt{A_j}, \quad (2)$$

with shape factor γ and cross-sectional area $A_j = h_j b_j$.

2.2 Tidal Inlet Morphodynamics

The evolution of the cross-sectional area of the tidal inlets is governed by the Escoffier (1940) principle based on a sediment balance for each inlet. It is assumed that the wave-dominated sediment import M_{sed} is a constant for all inlets, and independent of the inlet area. On the other hand, the tide-dominated sediment export is modelled with a cubic dependence on the tidal velocity amplitude U_j in the inlet, yielding $X_{sedj} = \alpha U_j^3$, with coefficient α. Setting up the sediment balance then yields

$$l\frac{dA_j}{dt} = X_{sedj} - M_{sed} = M_{sed}\left(\frac{U_j^3}{U_{eq}^3} - 1\right), \quad (3)$$

with U_{eq} the equilibrium velocity amplitude satisfying $M_{sed} = \alpha U_{eq}^3$. A hydrodynamic model is then required to find the velocity amplitudes U_j for each inlet j, which will be presented in the following two sections.

2.3 Inlet Hydrodynamics

The tidal oscillation in the sea is represented by a monochromatic tide, such that we can write for each inlet j

$$\eta_{oj} = Z\cos(\omega(t - t_j)) = \Re\left\{\hat{\eta}_{oj}\exp(i\omega t)\right\}, \quad (4)$$

with Z the tidal amplitude, ω the angular frequency of the tide and t_j the time shift of said tide, also contained in the complex amplitude $\hat{\eta}_{oj}$. Consequently, the flow velocity in the inlets u_j (positive from ocean to basin) can be represented by the single scalar complex amplitude $\hat{u}_j$, following $u_j = \Re\left\{\hat{u}_j\exp(i\omega t)\right\}$. Under the assumption that

the tidal inlets are narrow and short with respect to the tidal wavelength, the inlet flow can be modelled as spatially uniform, hence as one-dimensional in the direction of the inlet. This yields a linearly varying water level in the inlet, allowing the pressure gradient in the inlet to be expressed directly in terms of $\langle \eta_o \rangle_j$ and $\langle \eta_b \rangle_j$, denoting the water level averaged over, respectively, the ocean and basin end of the inlet. This average is defined as

$$\langle \eta \rangle_j = \frac{1}{b_j} \int_{R_j - \frac{b_j}{2}}^{R_j + \frac{b_j}{2}} \eta(r, \theta_j) dr. \tag{5}$$

Noting that the Froude number $\mathrm{Fr} = U_j / \sqrt{g h_j} \ll 1$, the inlet flow satisfies the linearised shallow water equations

$$\frac{\partial u_j}{\partial t} + \frac{r_j u_j}{h_j} = -g \frac{\langle \eta_b \rangle_j - \langle \eta_o \rangle_j}{l}, \tag{6}$$

with the second term the Lorentz (1922) linearisation for bottom friction in terms of friction coefficient r_j. Substituting the definitions of u_j and η_j in terms of their complex amplitudes (Equation 4) yields

$$\mathrm{i}\omega \hat{u}_j + \frac{r_j \hat{u}_j}{h_j} = -\frac{g}{l} \left(\langle \hat{\eta}_b \rangle_j - \langle \hat{\eta}_o \rangle_j \right). \tag{7}$$

Coupling the water motion in the basin to that in the inlet will yield an expression for $\langle \hat{\eta}_b \rangle_j$, allowing to solve for $\hat{u}_j$. The bottom friction coefficient is found following

$$r_j = 8 c_d U_j / 3\pi, \tag{8}$$

where the drag coefficient equals $c_d = 2.5 \cdot 10^{-3}$ and the characteristic velocity is chosen equal to the equilibrium velocity.

2.4 Basin Hydrodynamics

Analogous to the inlet hydrodynamics, the basin hydrodynamics is governed by the linearised depth-averaged shallow water equations, which, expressed in terms of the complex amplitudes of the basin elevation $\hat{\eta}_b$ and flow velocity $\hat{\mathbf{u}}_b = (\hat{u}_{br}, \hat{u}_{b\theta})$, read

$$\mathrm{i}\omega \hat{\eta}_b + \nabla \cdot (h_b \hat{\mathbf{u}}_b) = 0, \qquad \mathrm{i}\omega \hat{\mathbf{u}}_b + \frac{r_b \hat{\mathbf{u}}_b}{h_b} = -g \nabla \hat{\eta}_b, \tag{9}$$

explicitly allowing for spatially varying water elevation and flow velocities in the basin. The friction coefficient is found using Equation (8), again taking the equilibrium

velocity as characteristic velocity. Equation (9) is supplemented with the boundary conditions

$$\begin{aligned} \hat{\mathbf{u}}_b \cdot \mathbf{n} &= 0 & \text{at } \partial\Omega_{cl}, \\ h_b \langle \hat{\mathbf{u}}_b \cdot \mathbf{n} \rangle_j &= -h_j \hat{u}_j & \text{at } \partial\Omega_j, \end{aligned} \tag{10}$$

denoting a no-flow boundary condition at the closed boundaries $\partial\Omega_{cl}$, and a mass-continuity condition at the locations of all inlets. Here, $\mathbf{n}$ denotes the unit outward normal vector at the boundary. Finally, continuity of elevation and mass transport is demanded at the topographic steps, such that

$$\hat{\eta}_b^a = \hat{\eta}_b^b, \qquad h_b^a \hat{u}_{br}^a = h_b^b \hat{u}_{br}^b, \qquad \text{at } r = R^a, \tag{11}$$

$$\hat{\eta}_b^b = \hat{\eta}_b^c, \qquad h_b^b \hat{u}_{br}^b = h_b^c \hat{u}_{br}^c, \qquad \text{at } r = R^b, \tag{12}$$

with the superscripts denoting the depths and solutions in the different compartments in the radial direction.

3 Solution Procedure

The solution procedure is aimed to allow for the visualisation and analysis of the 3D vector field of the inlet evolution

$$\frac{d\mathbf{A}}{dt} = \left(\frac{dA_1}{dt}, \frac{dA_2}{dt}, \frac{dA_3}{dt} \right)^\top, \tag{13}$$

in the three-dimensional (A_1, A_2, A_3)-space, for which the analysis procedure is discussed in the next section. In this section, the model equations for the basin and inlets are reformulated to allow solving for $\hat{u}_j$, based on which the vector field can be computed using Escoffier's principle. This step introduces a strong nonlinearity in the solution, as the hydrodynamic model is linear but the inlet evolution is not.

The solution method is based on the linearity of the hydrodynamic model, allowing to express the basin elevation amplitude $\hat{\eta}_b$ as a sum of the contributions of all (source) inlets q. Averaging over an (action) inlet j then yields

$$\langle \hat{\eta}_b \rangle_j = \sum_q \langle \hat{\eta}_{bq} \rangle_j. \tag{14}$$

In line with Roos et al. (2013) and Reef et al. (2020), the basin impedances Z_{jq} are introduced, in an effort to express $\langle \hat{\eta}_{bq} \rangle_j = Z_{jq} A_q \hat{u}_q$, allowing the inlet momentum equations (Eqn. (9)) for a double inlet system to be expressed as the system of linear equations

$$\underbrace{\begin{bmatrix} \frac{\mathrm{i}\omega l}{g} \mu_1 + Z_{11} A_1 & Z_{12} A_2 & Z_{13} A_3 \\ Z_{21} A_1 & \frac{\mathrm{i}\omega l}{g} \mu_2 + Z_{22} A_2 & Z_{23} A_3 \\ Z_{31} A_1 & Z_{32} A_2 & \frac{\mathrm{i}\omega l}{g} \mu_3 + Z_{33} A_3 \end{bmatrix}}_{\mathbf{N}} \begin{pmatrix} \hat{u}_1 \\ \hat{u}_2 \\ \hat{u}_3 \end{pmatrix} = \begin{pmatrix} \hat{\eta}_{o1} \\ \hat{\eta}_{o2} \\ \hat{\eta}_{o3} \end{pmatrix}, \tag{15}$$

Here $\mu_j = 1 - \mathrm{i} r_j h_j^{-1} \omega^{-1}$ is introduced as a complex frictional correction factor. Provided that the basin impedances are all known, this system can be solved for

$\hat{u}_j$. To find these impedances, the Green's function for a point-source flow is first integrated over (source) inlet q, and consecutively averaged over (action) inlet j. To

8

achieve this, the equations governing the basin hydrodynamics (Equation (9)) are rewritten into

$$\nabla \cdot \left(\frac{h_b}{\mu_b} \nabla \hat{\eta}_b \right) + \frac{\omega^2}{g} \hat{\eta}_b = 0, \qquad \hat{\mathbf{u}}_b = \frac{g\mathrm{i}}{\mu_b \omega} \nabla \hat{\eta}_b. \quad (16)$$

Assuming that the basin elevation amplitude can be expressed in terms of the normalised eigenfunctions ψ_{mn} with corresponding eigenvalues λ_{mn}, which are derived in Appendix A, the response to delta-peak forcing can be written as the Green's function

$$G_b(r, \theta; r', \theta') = \sum_{m,n} \frac{h_b(r')}{\mu_b(r')} \frac{\psi_{mn}(r,\theta)\psi_{mn}(r',\theta')}{\lambda_{mn}}, \quad (17)$$

where a laterally uniform flow profile over the inlet mouth is assumed. Integration of G_b over inlet q then yields the basin elevation caused by said inlet:

$$\hat{\eta}_{bq} = \int_{R_q - \frac{b_q}{2}}^{R_q + \frac{b_q}{2}} \langle \nabla \hat{\eta}_b \cdot \mathbf{n} \rangle_q G_b(r, \theta; r', \theta_q) dr. \quad (18)$$

The width averaged basin elevation gradient can be expressed in terms of the inlet flow velocity amplitude by consecutively applying Equations (16) and (10) to find

$$\langle \nabla \hat{\eta}_b \cdot \mathbf{n} \rangle_q = \frac{\mu_b \omega}{g\mathrm{i}} \langle \hat{\mathbf{u}}_b \cdot \mathbf{n} \rangle_q = -\frac{\mu_b \omega h_q}{g\mathrm{i} h_b} \hat{u}_q. \quad (19)$$

Upon substitution, combined with applying the definition of the width integration, one then obtains

$$\hat{\eta}_{bq}(r, \theta) = \left[\frac{\omega \mathrm{i}}{g} \sum_{m,n} \frac{\psi_{mn}(r,\theta)\langle \psi_{mn} \rangle_q}{\lambda_{mn}} \right] A_q \hat{u}_q. \quad (20)$$

Averaging this result over inlet j, one then finally obtains

$$\langle \hat{\eta}_{bq} \rangle_j = \left[\frac{\omega \mathrm{i}}{g} \sum_{m,n} \frac{\langle \psi_{mn} \rangle_j \langle \psi_{mn} \rangle_q}{\lambda_{mn}} \right] A_q \hat{u}_q = Z_{jq} A_q \hat{u}_q, \quad (21)$$

yielding the final expression for the basin impedances Z_{jq}. For practical application, the summation is truncated to $m = 0, 1, ..., M$ and $n = 1, 2, ..., N$ with suitably chosen truncation numbers M and N.

4   Analysis Procedure

The solution procedure presented in Section 3 can be applied to produce a vector field, displaying the rate of change of the inlet areas $d\mathbf{A}/dt$ as a function of the inlet areas $\mathbf{A}$. An example of such a vector field is shown in Figure 3 for a double inlet system, where the lines visualise $dA_1/dt = 0$ (green) and $dA_2/dt = 0$ (red). Equilibria can be found at the intersections of these lines, allowing for stable equilibria (pink circles) and unstable equilibria (pink dots). The yellow and brown lines visualise the concept of inlet connectivity, which will be introduced later in this section. For systems with more inlets, the vector field also becomes increasingly complicated, as each inlet introduces one axis; hence, a triple inlet system will yield a three-dimensional vector field.
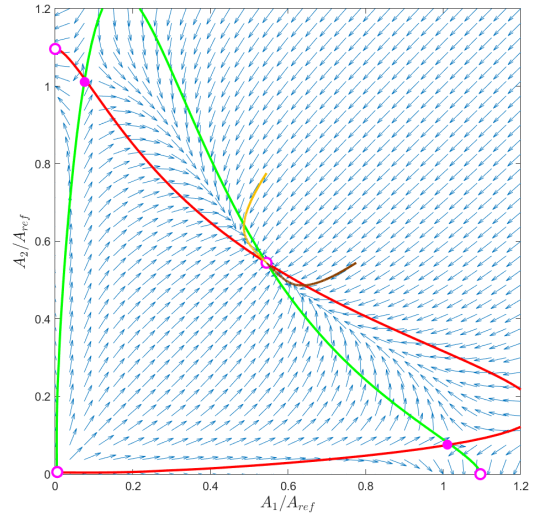

Figure 3: Visualisation of a flowchart for a double inlet system, displaying stable (pink circles) and unstable (pink dots) equilibria, laying on the lines $dA_1/dt = 0$ (green) and $dA_2/dt = 0$ (red). The concept of connectivity is illustrated with the brown (perturbing inlet 1) and yellow (perturbing inlet 2) lines.

Finding these equilibria, however, turns out to be a difficult task, in particular for triple inlet systems as there is one more dimension to be considered. To find the equilibria, a numerical search algorithm is designed that divides the vector space into a number of different boxes. In case the signs of all components of $d\mathbf{A}/dt$ change within the box, it can potentially contain an equilibrium and the box is refined. The procedure is then repeated until the equilibrium is known with sufficient accuracy. However, this approach introduces two complications, the first resulting from the fact that the Escoffier principle breaks down on planes where $A_j = 0$ for one j, or axes where $A_j = 0$ for two j. This is a consequence of the assumption that M_{sed} is constant regardless of the inlet area. Consequently, a sediment import remains present also if the inlet closes, hence the equilibrium tracking algorithm needs to be restricted to these planes/axes in order to find the correct equilibria located on them. Secondly, the equilibrium tracking algorithm is not guaranteed to find all equilibria. For example, when equilibria are located close to one another, it goes easily unnoticed as no sign-change is detected within a box. This is an important limitation to be kept in mind when interpreting the results.

Once the equilibria are found, their stability can be analysed by linearising the vector field in the vicinity of said inlet following

$$\frac{d\mathbf{A}'}{dt} = \mathbf{J}\mathbf{A}', \quad (22)$$

with $\mathbf{J}$ the Jacobi matrix of the vector field (found in Appendix C) and $\mathbf{A}' = \mathbf{A} - \mathbf{A}_{eq}$ the difference between the cross-sectional inlet area and the cross-sectional inlet area in equilibrium ($\mathbf{A}_{eq}$). Computing the eigenvalues Λ_i and eigenvectors $\mathbf{v}_i$ then yields an insight into the stability of the equilibrium, as it is considered stable if $\Re\{\Lambda_i\} < 0 \ \forall$ i. Additionally, these eigenvalues and eigenvectors can be
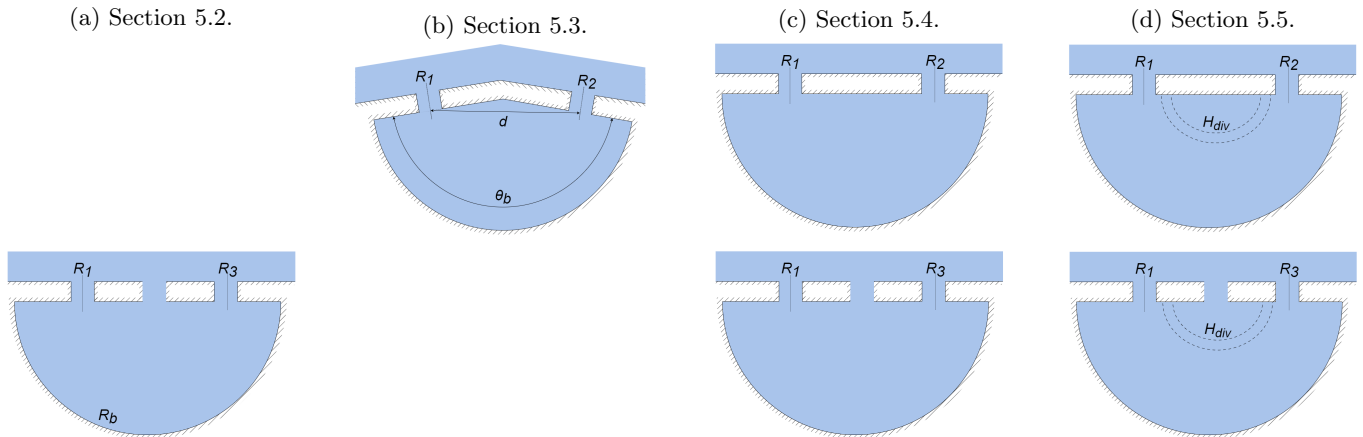
Figure 4: Visualisation of the different simulations performed in this study. Top row indicates double inlet systems, bottom row triple inlet systems. Included parameters denote the parameters varied in that simulation. In Figure 4b, also the distance parameter d is included.

used to write any trajectory $\mathbf{A}'(t)$ in the vicinity of the equilibrium as

$$\mathbf{A}'(t) = \sum_i c_i \mathbf{v}_i \exp(\Lambda_i t), \qquad \sum_i c_i \mathbf{v}_i = \mathbf{A}'_0, \quad (23)$$

where $\mathbf{A}'_0 = \mathbf{A}'(0)$. Given this expression for the trajectory, the connectivity is easily computed following the definition by Roos & Schuttelaars (to be published) as

$$C_{jq} = \frac{A'_j(t^*)}{\Delta A_q}, \qquad (24)$$

with ΔA_q denoting the initial perturbation of inlet q and $A'_j(t)$ denoting the trajectory of the disturbance of inlet j, where solely inlet q is perturbed and all others are not. An example of these trajectories is given in Figure 3, where the brown line displays the trajectory after perturbing inlet 1, whilst the yellow line displays the trajectory upon perturbing inlet 2. Furthermore, t^* is defined such that $|A'_j(t^*)|$ is maximal. This connectivity quotient expresses the perturbation of inlet j relative to an initial perturbation of inlet q. We note that this definition only applies to stable equilibria, i.e. equilibria for which all eigenvalues are negative. Furthermore, the connectivity is symmetric in case $C_{jq} = C_{qj}$, and asymmetric if this is not the case.

In the visualisations that follow, the inlet areas are normalised against a reference inlet area, being the inlet area in a single inlet system without tidal amplification and bottom friction and under the assumptions that the tidal forcing is applied directly at the boundary of the domain and that there is no spatial variation in the water level elevation in the basin ('pumping mode'). Under these assumptions, Equation (15) reduces to

$$\frac{\omega \mathrm{i}}{g} \frac{\langle \psi_{01} \rangle_1^2}{\lambda_{01}} A_1 \hat{u}_1 = Z, \qquad (25)$$

where it is easily found that

$$\langle \psi_{01} \rangle_1^2 = \frac{2}{R_b^2 \theta_b h_b}, \qquad \lambda_{01} = -\frac{\omega^2}{g h_b}. \qquad (26)$$

Upon substitution Equation (26) in (25), multiplying the result with its complex conjugate and using the definition that, in equilibrium, $|\hat{u}_1| = U_{eq}$, one finds that

$$A_{ref} = \frac{\theta_b R_b^2 Z \omega}{2 U_{eq}}. \qquad (27)$$

5 Results

In this section, the influences of different parameter variations on the model results are explored. We systematically explore the effect of the basin dimensions in a sectoral-shaped geometry by varying the basin angle θ_b for a double inlet system and the basin-radius R_b for a triple inlet system. These analyses are combined with symmetrically varying the inlet location, i.e. varying $R_1 = R_2$ for a double inlet system and $R_1 = R_3$ for a triple inlet system. In a triple inlet system, the restriction to a symmetric case implies that inlet two must be centered around the origin of the coordinate system, thus also restricting the basin angle to $\theta_b = 180°$, as shown in Figure 1c. Additionally, for both a double and triple inlet system, symmetry in the forcing conditions of the inlets is demanded. The restriction to a symmetric system is chosen to reduce the computational demand of the equilibrium tracking algorithms, whilst still allowing for the complex behaviour of the system to be explored. The effect of the transition from a double to a triple inlet system is further highlighted by solely varying the symmetric inlet location. Finally, the effect of the tidal divide is explored by varying the tidal divide height in combination with the symmetric inlet location for a double and triple inlet system. A visualisation of all the different simulations is given in Figure 4.

All results are obtained with the same default parameters, chosen to highlight key features of the system's behaviour, which are only varied in case the effect of the parameter is explored. This was the main motivation behind selecting these values, although they do exhibit some

Table 1: Default parameter values. In case $H_{div} = 0$, the location of the topographic steps $R^{a,b}$ have no physical meaning. The symmetry of the system becomes apparent by choosing R_i symmetrically, and r_i, Z, t_i the same for all inlets.

R_b	Basin radius	14	km	l	Inlet length	5	km
θ_b	Basin angle	180	°	γ^2	Inlet shape factor	0.005	-
h_b	Basin depth	5	m	R_i	Radial inlet coordinates	$(10, 0, 10)$	km
H_{div}	Tidal divide height	0	m	θ_i	Axial inlet coordinates	$(0, 0, \theta_b)$	rad
$R^{a,b}$	Radial coordinates topographic steps	5,6	km	r_i	Friction coefficient in inlets	0.0021	m s^{-1}
r_b	Bottom friction coefficient in basin	0.0021	m s^{-1}	t_i	Tidal time shift (all inlets)	0	s
Z	Tidal amplitude in ocean	1	m	M	Axial truncation number	10	-
U_{eq}	Equilibrium flow velocity amplitude	1	m s^{-1}	N	Radial truncation number	10	-

similarities with the Western Wadden Sea system. The parameter values are given in Table 1 and yield a reference area of the inlets of $A_{ref} = 4.33 \cdot 10^4$ m^2, although it should be noted that this varies for some simulations due to varying values of R_b or θ_b. The connectivity quotient is analysed for the unique non-trivial equilibrium state in which all inlets are open. As a consequence of the symmetric, the connectivity quotients satisfy $C_{12} = C_{13}$, $C_{21} = C_{31}$ and $C_{23} = C_{21}$ for a triple inlet system.

5.1 Existence of Equilibria

The first key result of this study is that there exists a stable equilibrium with all three inlets open for a large number of parameter settings. The effect of the different parameters is explored in Sections 5.2 till 5.5; in this section, an example of such a system is provided and used to illustrate how the results in the following sections are obtained.

In Figure 5, an example of a three-dimensional vector field is provided but plotted on logarithmic scales. For readability, the vectors are omitted. The isoplanes $dA_1/dt = 0$ (green), $dA_2/dt = 0$ (red) and $dA_3/dt = 0$ (blue) are plotted, but only where they intersect the planes where one $A_i = 0$, again to foster readability of the figure. At the intersection of all three isoplanes, the equilibria can be found, which are either stable (pink circles) or unstable (pink dots). From this figure, it can be concluded that a total of 27 equilibria is present in the system, of which eight are stable: one with all inlets closed, three where one inlet is opened (one for each inlet), three where two inlets are opened (for all combinations of inlets), and one where three inlets are opened. The complete behaviour of the system is, however, quite difficult to visualise, as visualising three-dimensional vector fields is challenging in itself. Furthermore, this figure also illustrates the difficulty in finding all equilibria: if equilibria are located close to one another, they easily go unnoticed.

For the analysis of the key system behaviour, this study therefore focuses on the unique non-trivial equilibrium state for which all inlets in the double or triple inlet system are open. In the next sections, we investigate the influence of various parameter variations on the cross-sectional areas of the inlets in this particular state, as well as the connectivity quotients in case this equilibrium is stable. These areas and connectivity quotients can con-
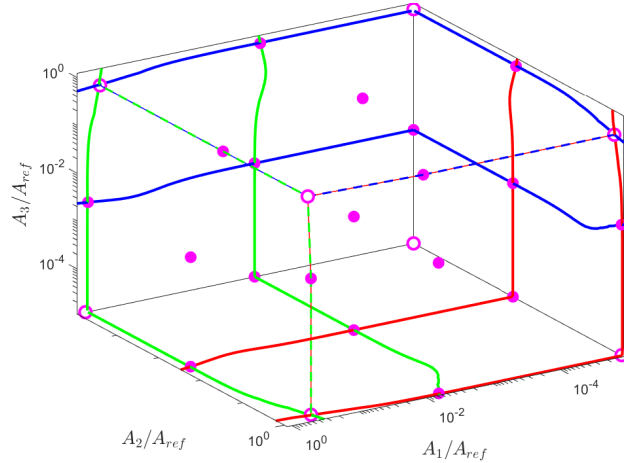

Figure 5: Visualisation of all the equilibria in a 3D flow field. On the planes where one $A_i = 0$, the projections of the planes $dA_1/dt = 0$ (green), $dA_2/dt = 0$ (red) and $dA_3/dt = 0$ (blue) are shown. On the intersects, stable (pink circles) and unstable (pink dots) are found.

sequently be visualised as a surface plot to visualise the influence of the parameters, as done in for instance Figures 6, 8, 10 and 11. It should thus be highlighted that each point corresponds to a vector field like the one in Figure 5, yet with different locations and properties of the equilibria.

5.2 Effect of Basin Radius

First, the influence of the basin radius on inlet connectivity is explored for a triple inlet system, in combination with the effect of symmetrically varying the inlet location. The results of this analysis are presented in Figure 6, where no connectivity values exist in the white space (where the equilibrium is unstable) and in the hatched regions (where inlets either overlap or extend beyond the domain boundary). In Figure 6d till 6f, it is seen that the dimensionless cross-sectional inlet area A_i/A_{ref} stays roughly constant for varying R_b, indicating that the inlet areas are directly dependent on the basin area. Logically, the cross-sectional area of the middle inlet A_2 (Fig. 6e) decreases in area when the other two inlets are located closer and grows when the inlets are located further away, shown by the strong horizontal variation of the inlet area in the figure. This results from the fact that less (more)
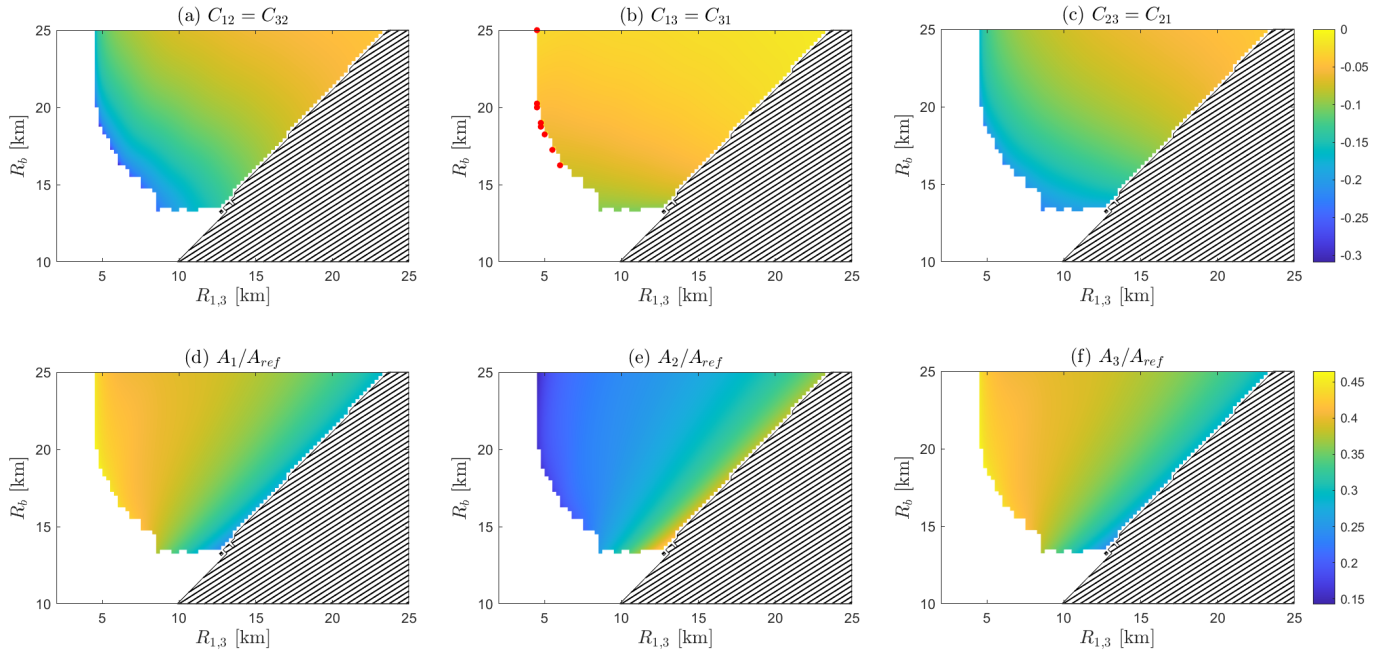
Figure 6: Effect of varying basin radius R_b and symmetric inlet location $R_{1,3}$ on the connectivity (top row) and inlet size (bottom row) in a triple inlet system. Red dots in Figure 6b denote a positive connectivity quotient.

water is drained via the middle inlet when other inlets are located closer (farther). Conversely, the other two inlets decrease in area with increasing inter-inlet distance (Fig. 6d and 6f, also the horizontal variation).

Furthermore, Figures 6a till 6c show that, when increasing the radial coordinate of the outer two inlets (horizontal axis), all connectivity quotients increase. Hence, an increasing inter-inlet distance logically yields a less negative connectivity quotient, hence decreasing inlet connectivity. It can also be observed that an increasing basin radius (vertical axis), hence increasing basin size, yields reduced inlet connectivity. Finally, all panels in Figure 6 show that, for a larger basin radius and thus basin area, the inlets can be located closer to one another, without causing the system to become unstable. This is shown by the fact that the boundary between coloured and white space in the figures, i.e. the boundary between resp. stable and unstable equilibria, is located at lower values of $R_{1,3}$ for increasing R_b. It should, however, be noted that the exact location of this boundary is not completely certain, as the used equilibrium tracing algorithm can have some difficulty in case equilibria are close to one another or very close to becoming unstable. This explains the rather ragged shape of the boundary between stable and unstable and of the hatched area, and the occurrence of a small stable "island" for small R_b.

An interesting observation is that, for the combination of $R_b = 25$ km and $R_{1,3} = 4.5$ km, the inlet connectivity $C_{13} = C_{31}$ suddenly turns positive, a behaviour shared by a few other parameter combinations appearing and shown as red dots at the boundary of stability in Figure 6b. This behaviour is further explored in Figure 7, showing that the trajectory of inlet 1 (or 3) upon perturbing inlet 3 (or 1) displays two bends, of which the

positive extremum is larger than the negative. Consequently, the connectivity becomes positive, and the value changes abruptly in Figure 6b: as the connectivity is defined as the maximal value, the positive extremum can be present in other parts of Figure 6b as well, but goes unnoticed as it is smaller than the negative extremum. As such, the observed behaviour is a correct model result, but the current definition of connectivity does not detect this behaviour.

5.3 Effect of Basin Angle

The effect of transitioning to a radial coordinate system is further explored by varying the basin angle θ_b. As this parameter variation introduces a kink in the coastline at the origin, it does not allow for an inlet centered around this point, hence this analysis is performed for a double inlet system in which the inlet locations are symmetrically varied (illustrated in Figure 4b). In Figure 8, the inlet connectivity (Fig. 8b) and the cross-sectional inlet area (Fig. 8a) are displayed for varying inlet locations and basin angles, revealing that the smaller the basin angle (vertical axis), the larger the radial coordinate of both inlets (horizontal axis) needs to be before a stable situation is reached, again visualised by the transition from a coloured to white plane. In a stable situation, the inlet area turns out to be directly correlated to the basin angle and hence the basin area, whilst only minimally varying as a result of the inlet location. However, a large influence of the basin area on inlet connectivity can be observed, which is not surprising as both variables influence the linear distance between both inlets. This behaviour is further explored in Figure 8c, showing the inlet connectivity as a function of basin area (horizontal axis) and the linear distance $d = 2R_{1,2} \sin(\theta_b/2)$ between the inlets (see Figure
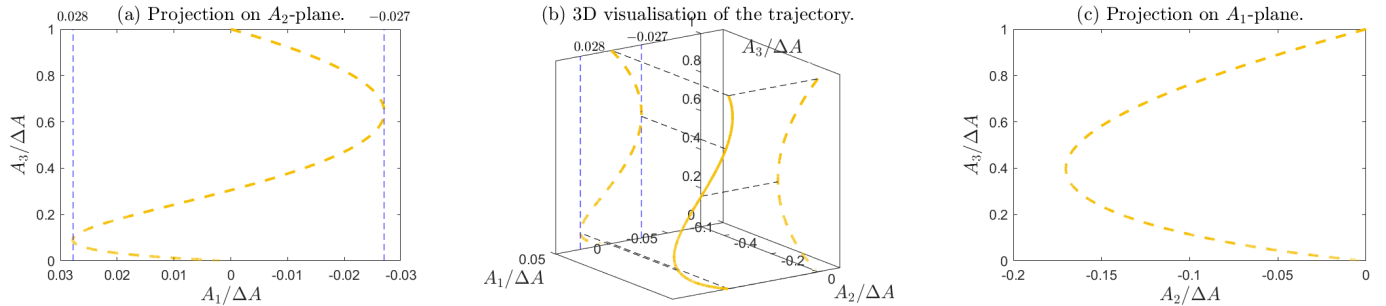
Figure 7: Display of the trajectory back to the equilibrium when perturbing A_3 for $R_b = 25$ km, $R_{1,3} = 4.5$ km. In the middle (b) a three-dimensional visualisation, with projections on the A_2-plane (panel a) and A_1-plane (panel c).

4b) on the vertical axis. From Figure 8c, it becomes apparent that the inlet area and inter-inlet distance independently influence the inlet connectivity: both larger inlet distancing and larger basins lead to a less negative connectivity quotient, hence reducing the connectivity. This is in line with the conclusions from the previous section, where increasing the basin area (realised by varying R_b) and the inter-inlet distance (realised by only varying $R_{1,3}$) also reduced the inlet connectivity, albeit for a triple inlet system. It also becomes apparent that the maximal value of the connectivity quotient equals $|C_{jq}| \leq \frac{1}{2}$, an upper bound also found for double inlets with a square basin by Roos & Schuttelaars (to be published).

5.4 Double to Triple Inlet System

To investigate the influence of the basin angle θ_b while maintaining symmetry, it was required to change the number of inlets in the system. In this section, we highlight the effect of reducing the number of inlets from three to two by showing how the inlet connectivity changes as a function of the symmetric inlet location $R_{1,2}$ (double inlet system) and $R_{1,3}$ (triple inlet system). Both analyses are applied for a basin angle of $\theta_b = 180°$, where the middle inlet in the triple inlet system is centered around the origin. From Figure 9, it becomes apparent that the general behaviour of the system does not change when transitioning from a double (top) to a triple (bottom) inlet system: the connectivity quotient (blue axis) between inlets becomes less negative with increasing inlet distance (horizontal axis), hence the connectivity between the inlets reduces. For a triple inlet system, it becomes clear that the closest inlets are most strongly connected (dashed and dotted blue lines), while combinations of inlets which are not directly adjacent (solid blue line) are less connected. However, there are a few key differences between a double and triple inlet system, the first being that the theoretical upper bound of $|C_{jq}| < \frac{1}{2}$, which is approximated for a double inlet system, is no longer approximated for a triple inlet system. It should, however, be noted that this behaviour is exhibited by the system when it is on the verge of stability, a situation in which the equilibria are located close to one another and hence the tracking algorithm has large difficulty finding the stable equilibrium. Secondly, the connectivity between the closest two inlets (one and two, and two and three) has become asymmetrical for a triple inlet system. This is readily explained

by the fact that inlets one and two are not symmetrically located, hence a symmetrical connectivity quotient should not be expected. The inlets that are located symmetrically (one and three in a triple inlet system) also display a symmetrical connectivity quotient ($C_{13} = C_{31}$), as expected. Additionally, the figure reveals that the inlets in a double inlet system can be located much closer than in a triple inlet system, an observation that can logically be explained by the fact that the basin area for both inlets is the same. Hence, each inlet drains a much larger area in a double inlet system compared to a triple inlet system. This is in line with the results from Figures 6 and 8, where it is also shown that larger basin areas can enable inlets to be located closer to one another.

In terms of inlet areas, Figure 9a reveals that the inlet location in a double inlet system barely has any influence on the size of the inlets (nearly horizontal orange line). However, this drastically changes for a triple inlet system, where locating the inlets further outward reduces the size of the outer two inlets (solid orange line, Figure 9a) and increases the size of the inner inlet (dashed orange line). This is quite logical as the water will generally be drained by the closest inlet; locating the symmetrical inlets further outwards will decrease the area they can drain (as they lose area in the middle of the system), hence reducing the size of the two inlets. Conversely, the middle inlet grows to still accommodate the draining of the full basin. Also for varying basin radius (and thus basin size), this behaviour is displayed by the system. The results (not shown here) show that, irrespective of the basin radius, the middle inlet will be larger than the outer two if $R_{1,3}/R_b \lesssim 0.67$; elsewhere, the outer two inlets will be larger. However, the exact difference between the cross-sectional areas is strongly depending on the basin radius and inlet location.

5.5 Effect of a Tidal Divide

Finally, the effect of the presence of a circular tidal divide around the origin is investigated for a double (Figure 10) and triple (Figure 11) inlet system. Before presenting and interpreting these results, it must be noted that for relatively high tidal divides ($H_{div}/h_b > 0.75$, not shown here), the error in the normalisation of the eigenfunctions,
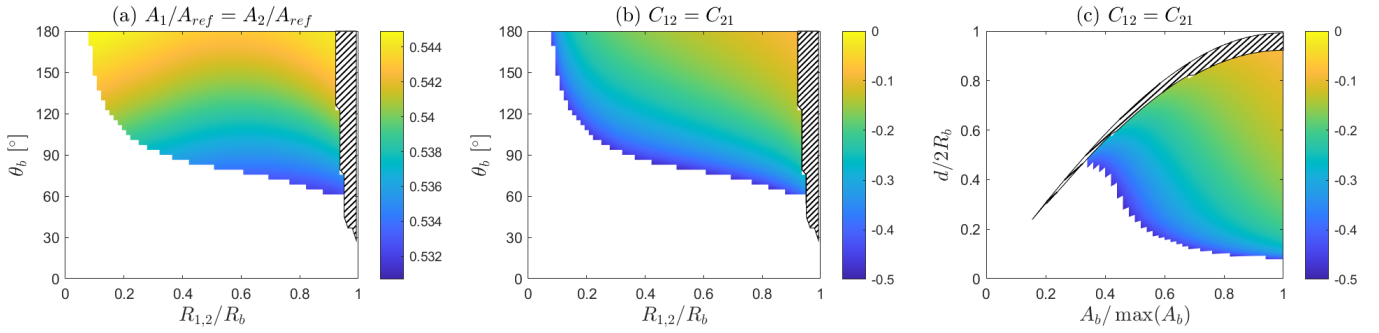
Figure 8: Effect of varying basin angle θ_b and symmetric inlet location $R_{1,2}$ on the inlet area (left, a) and connectivity (middle, b) in a double inlet system. On the right (c) a visualisation of the connectivity as a function of basin area and inlet distance.
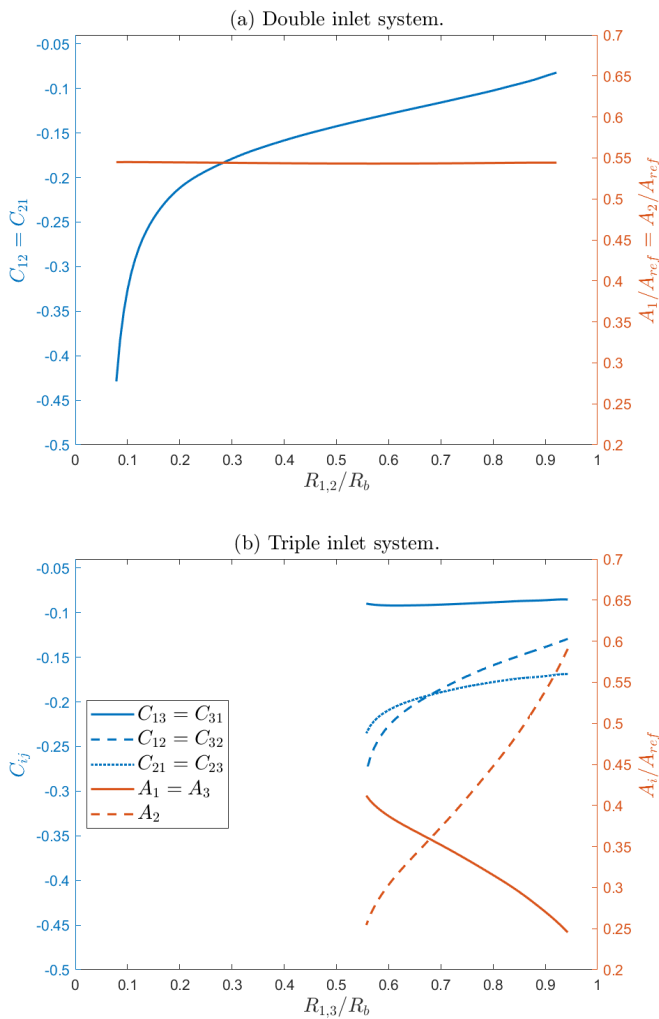

Figure 9: The inlet connectivity (left, blue axes) and inlet size (right, orange axes) as a function of the inlet location for a symmetric double (top panel, a) and triple (bottom panel, b) inlet system. Where no curve is plotted, no stable equilibrium exists (small $R_{1,2}$ and $R_{1,3}$), or the inlets extend beyond the domain boundary (large $R_{1,2}$ and $R_{1,3}$).

defined as

$$E = \max_{m,n_1,n_2} \left[\int \frac{r h_b(r)}{\mu_b(r)} \psi_{mn_1} \psi_{mn_2} d\Omega \right], \qquad (28)$$

increases with increasing tidal divide height, as shown in Figure 10c. There is machine precision error present when the tidal divide is absent, but increasing the tidal divide height also yields a significant increase in the error. As such, the results presented here should be interpreted with this development of the error in mind: the higher the tidal divide, the more uncertainty whether the results represent physical reality, or are introduced by this error. With this in mind, we can make some statements about the behaviour for, roughly, $H_{div}/h_b < 0.4$.

For a double inlet system, Figure 10a shows that both the inlet location (horizontal axis) and the presence of a tidal divide (vertical axis) barely influence the size of both inlets. The former is in line with earlier conclusions, but the latter comes as a surprise as one would expect that the presence of a tidal divide limits the basin area that can be drained by both inlets. After all, a very high divide practically reduces the basin to solely the outer ring. Such behaviour is gently shown in Figure 10a by the slightly reducing inlet area in the vertical direction, yet this only becomes more pronounced for larger tidal divide heights. As this coincides with an increasing error in the orthonormalisation of the eigenfunctions, it is difficult to draw conclusions about whether the observed behaviour is caused by the aforementioned physical phenomenon or a result of the increasing error. However, seeing the plausible physical explanation and the gentle reduction of inlet area for small tidal divides, the observed reduction of inlet area could very well be the result of mentioned physical phenomenon.

In terms of inlet connectivity, both increased inlet distance (horizontal axis) and increased tidal divide height (vertical axis) yield a less negative connectivity quotient, hence a reduction in the connectivity of the two inlets. The former is in line with earlier conclusions, the latter can logically be explained by the fact that the increased tidal divide height will also increase the effect of bottom friction and reduce the water depth available for exchanging water over the tidal divide. Both mechanisms limit the
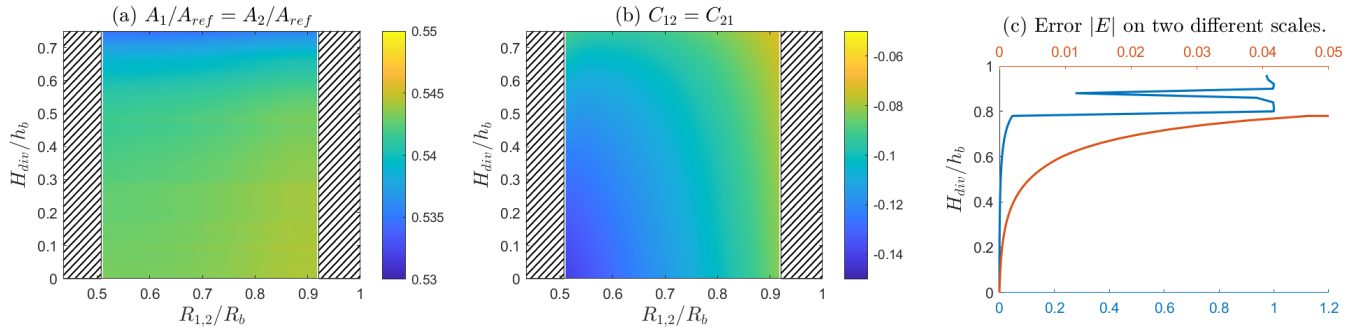
14

Figure 10: Effect of varying the tidal divide height H_{div} and symmetric inlet location $R_{1,2}$ on the inlet size (left panel, a) and inlet connectivity (middle panel, b). On the right (c) the maximal error in the orthonormality.

exchange of water over the tidal divide and hence reduce the connectivity between the inlets at either side of the divide.

For the triple inlet system (Figure 11), the radial location of the two outer inlets has a significant influence on the connectivity and inlet areas as also concluded earlier. Based on the results, it is concluded that the presence of a tidal divide generally limits the portion of the basin drained by the central inlet (2), as an increased tidal divide reduces the inlet area A_2 in all cases (Fig. 11e), whilst increasing the cross-sectional area of the outer two inlets (Fig. 11d and 11f). It is, however, anticipated that the radial location of the tidal divide has a strong influence on this, as simulating a divide with a larger radius will increase the area that will be drained by inlet two. This hypothesis, however, cannot be substantiated with the presented data and requires further research. In the figure, however, it is seen that locating the outer two inlets further away, will again increase the cross-sectional area of the middle inlet (the horizontal variation in Figure 11e), implying that the middle inlet in these cases drains water over the tidal divide. As such, it is concluded that the increase of the tidal divide height gradually reduces the amount of water exchanged over the tidal divide, in this case limiting the discharge through the middle inlet and hence its cross-sectional area.

In terms of inlet connectivity, it is seen that the increase of the tidal divide height has an asymmetrical effect on the connectivity between the middle and the outer two inlets. By comparing results in the vertical direction, Figure 11a shows that the inlet connectivity $C_{12} = C_{32}$ (inlet 2 is perturbed) is barely changing when increasing the tidal divide height, whereas the connectivity $C_{23} = C_{21}$ (inlet 1 or 3 is perturbed) is influenced much more (Figure 11c). The physical mechanism behind this is further discussed in Section 6.1.

Additionally, it is observed that the connectivity quotient between the outer two inlets (Figure 11b), which was already close to zero, becomes less negative when increasing the tidal divide height. This can logically be explained by the fact that the tidal divide forms a barrier forcing the exchange of water to take place more around the barrier rather than over the barrier. This increases the distance the water travels, hence reducing the connectivity. Con-

sequently, it is not anticipated that the inlet connectivity tends to zero as the tidal divide height approximates the water depth; after all, the water can still (freely) travel around the divide, although the longer distance that is to be covered will reduce the inlet connectivity.

6 Discussion

6.1 Physical Mechanisms

In the previous sections, two important results were presented: with increasing basin area, be it by increasing R_b for a triple inlet system (Sec. 5.2) or by increasing θ_b for a double inlet system (Sec. 5.3), the connectivity between all inlets decreases. Secondly, the triple inlet system allows for asymmetrical connectivity between inlets (i.e. $C_{12} \neq C_{21}$), even with a tidal divide present (see Fig. 11a and 11c). This is also observed in Figure 9b, where it is even observed that the asymmetry in the connectivity switches when the inlets are located further outward as the blue dashed and dotted lines intersect. This seems to coincide with the intersection of the orange solid and dashed lines, hence suggesting that the asymmetry in the inlet areas is the determinant of the asymmetry in the inlet connectivity. This is supported by Figure 12a, where the fraction C_{12}/C_{21}, a measure of asymmetry in the connectivity responses, is plotted against A_1/A_2, a measure of asymmetry in inlet sizes. From this figure, it appears that $C_{ij} > C_{ji}$ if $A_i > A_j$, which should physically be interpreted as the smallest of the two inlets having a more significant influence on the larger inlet than the larger inlet has on the smallest. As this figure includes the data for various tidal divide heights and inlet locations, it can also be concluded that the tidal divide height or inlet location barely has an influence on this conclusion.

However, it turns out that the basin size has a significant influence on this relation, see Figure 12b. Here, the data for various basin radii (Sec. 5.2) is also scattered, again confirming a direct relationship between asymmetry in tidal inlet size and asymmetry in connectivity. However, this relationship can be different depending on basin area: for smaller basins, the smallest inlet is connected more strongly to the larger inlet than vice versa: $C_{ij} > C_{ji}$ if $A_i > A_j$. This is also the relation as displayed in Figure
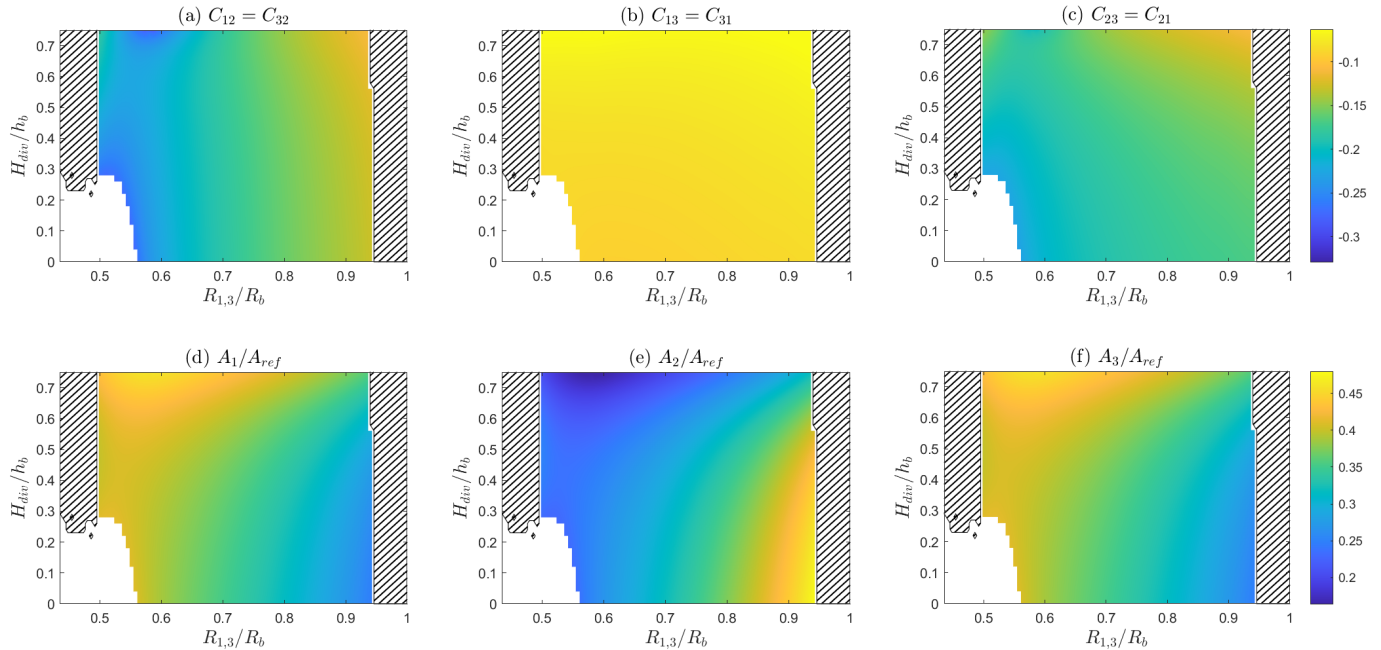
15

Figure 11: Effect of varying the tidal divide height H_{div} and symmetric inlet location $R_{1,3}$ on the connectivity (top row) and inlet size (bottom row) in a triple inlet system.

12a, which is generated with a small basin. However, for larger basins, the smallest inlet is connected weaker to the largest inlet than vice versa: $C_{ij} > C_{ji}$ if $A_i < A_j$. The explanation for this can be found in the two mechanisms presented by Roos et al. (2013).

For smaller basins, inlets will generally be smaller and thus shallower, hence the effect of bottom friction in the inlets will be large. As the bottom friction in the inlets is inversely proportional to the inlet depth, a change in the inlet area will result in a larger change in bottom friction in shallower inlets. This then leads to a change in inlet flow velocity, which in turn leads to a change in the basin elevation amplitude, which then influences the other inlets. It can thus be concluded that the inlet that causes the largest change in basin elevation will have the largest connectivity, which is the shallowest and thus smallest inlet in a system with a small basin.

On the other hand, if the basin is much larger, the inlets will be much larger and bottom friction in the inlets will play much less of an influence. Instead, the response of the system can be explained with the changes in pressure gradient: in the largest inlet, the bottom friction will play the smallest role, hence the pressure gradient will change most as a result of changing the inlet areas. This will foster a change in inlet flow velocity, which in turn changes the basin elevation amplitude. Hence, the largest inlet will display the strongest connectivity.

It should be noted here that only the asymmetry in connectivity C_{12}/C_{21} has been considered so far. The effect of the basin area on the connectivity in absolute sense is also investigated and visualised in Figure 12c, where it can clearly be observed that the connectivity overall reduces with increasing basin area, as was already highlighted in Sections 5.2 and 5.3 for respectively a triple- and double inlet system. This is direct consequence of the first mechanism: the larger the inlets, the lower the effect of bottom friction in the inlets. Consequently, a change in inlet area will simply lead to slightly increased flow velocities in that inlet, limiting the change of tidal prism and thus the change in basin elevation amplitude. As a consequence, the basin elevation at the other inlets will not change much, reducing the connectivity in the system.

Hence, it is concluded that the inlet connectivity is a result of a complex interaction between inlets and basin, where basin area and the presence of tidal divides each play their role. However, it can also be concluded that the asymmetry in inlet connectivity is almost entirely a consequence of asymmetry in cross-sectional inlet area, and that the basin only plays a role in this via the asymmetry of the inlets. It should, finally, be noted that this asymmetry need not be limited to asymmetric location; also asymmetric forcing and shaping of the inlets can have these effects. This conclusion would, however, suggest that choosing a combination of these factors, such that the inlet location is asymmetric but the inlet cross-sectional areas are the same, would yield symmetric connectivity again. This is, however, to be researched further.

6.2 Wadden Sea

It should be noted that the parameters used in this study to some extent represent the Western Wadden Sea system (for instance in basin depth and tidal amplitude) but that a few drastic simplifications were made in this study: a symmetric system is assumed, forcing a basin angle of $180°$, and the used basin radius is much smaller than in reality. As such, the basin area in reality will be much
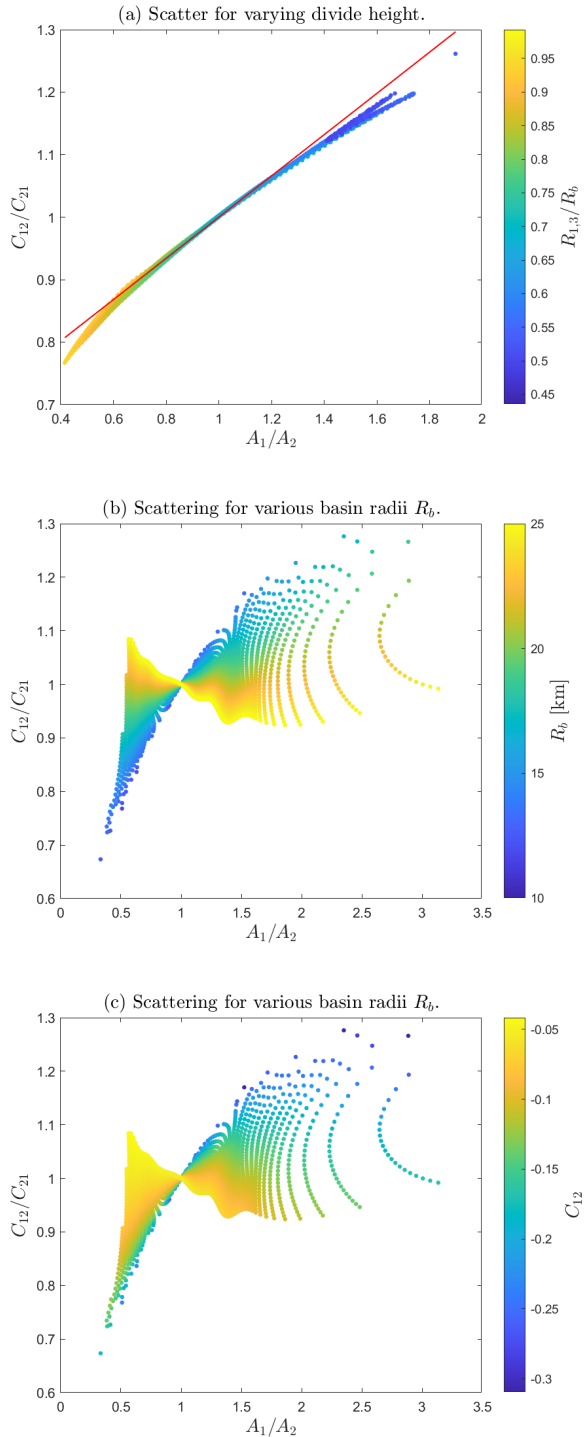
Figure 12: Scattering C_{12}/C_{21} against A_1/A_2 for various tidal divide heights (top (a), data from Figure 11) and for various basin radii (bottom two (b,c), data from Figure 9). We highlight the different meanings of the color bars here.

larger and allows the inlets to be located much farther apart. Hence, it is recommended to further investigate the influence of asymmetry on the stability and connectivity properties of a triple inlet system, after which also the influence of the basin angle can be investigated. The presented results, however, do allow for some qualitative conclusions about the Western Wadden Sea system.

The present study confirms that systems like the Western Wadden Sea, with a similar circular geometry, can be in equilibrium with three open inlets. The presented model results show that the larger the basin, the more robust the system becomes as inlets can be located closer to one another (Fig. 6). As the Western Wadden Sea has a larger basin and has the inlets located farther apart, it can safely be concluded that the model will also predict that a stable equilibrium with all three inlets open is possible in the Western Wadden Sea. Extrapolating the results from Figure 6 would then also imply that all the connectivity quotients will be close to zero, as a result of the larger basin and the larger inter-inlet distance. The model results would thus suggest that the inlet system of the Western Wadden Sea is rather robust, where short-term perturbations of one of the inlets will not yield large disturbances of the other inlets. The presented results, therefore, suggest that the Western Wadden Sea is relatively resilient to local perturbations of the inlets.

Additionally, the results shown in Figure 11 display the effect of the tidal divide present around the Eierlandse Gat inlet, displaying reduced connectivity with the other inlets for increasing tidal divide height. This is moderately in line with the conclusions from Zimmerman (1976), suggesting a limited exchange of water over the divide. However, the presented results still suggest a significant connectivity quotient for larger divide heights ($H_{div}/h_b \approx 0.4$), implying there still is a significant exchange of water over the divide. This can either be caused by the introduced normalisation error in the model (Fig. 10c), but can also be a consequence of the chosen dimensions to parameterize the tidal divide. After all, increasing the radial location of the divide will reduce the amount of water being forced over the divide, whereas increasing the tidal divide width will increase the effect of bottom friction, hence reducing the tidal prism over the divide. The effect of these two parameters should therefore be further investigated.

Furthermore, the symmetric configuration of the inlets in the presented simulations forced a basin angle of 180° to be used, whereas the Western Wadden Sea can better be approximated with an angle of roughly 130° (see Fig. 1b). This shift will reduce the direct distance between the outer two inlets as also explained in Section 5.3. As such, the inlet connectivity between the outer two inlets will change relatively a lot as a consequence of this transition, although this connectivity quotient will still be relatively low due to the large basin and inter-inlet distances. This is, however, to be further investigated.

Finally, the chosen solution strategy does not allow for an axial tidal divide to be present in the system (green in Figure 1b). This is a major simplification compared

to the Western Wadden Sea system. However, the results in Figure 11b display a very weak connection between the outer two inlets, even in absence of this tidal divide. This suggests that including an axial tidal divide will not change the connectivity between these two inlets, but this statement cannot be further investigated with these results and this model.

6.3 Limitations

The omission of the axial tidal divide mentioned in the Introduction and Section 6.2 is an important physical limitation of the model applied. More generally, the system of interest was strongly schematised and only the essential processes were included in the process-based model, leading to the omission of for instance the interaction between the ocean and inlets, the linearisation of the bottom friction and the demand for symmetry (in both the forcing and the inlet locations) in the model. However, despite these assumptions, the developed model is able to capture key processes of the barrier coast and allows to simulate stable equilibria with multiple inlets open, which is in line with the conclusions from Roos et al. (2013). Besides, it allowed for the interpretation of the presented results in terms of the key physical mechanisms that were included in the model.

An important numerical limitation to all the presented results is the truncation of the infinite sums in Eqn. (21), leading to a trade-off between accuracy and computational speed when choosing the values for M and N. For the smaller basins, a convergence analysis has shown that the chosen values are appropriate, but this may become less when the basin size increases. It is therefore expected that the wave-like pattern in Figure 12b is caused by the limited number of radial modes N included in the simulation. Practically, it was not possible to increase the number of modes for this simulation due to the computational power available, but this may be worth considering if more computational power is available.

The simulations containing a tidal divide in the system (Sec. 5.5) also contain a different error, being the error in the orthonormalisation of the eigenfunctions as shown in Figure 10c: the higher the tidal divide, the larger the error in the orthonormalisation. Hence, the results including a tidal divide should be interpreted with this error in mind, although the error is believed to be small enough to allow for qualitative conclusions about the behaviour of the system, particularly for smaller divides ($H_{div}/h_b < 0.4$). It is, however, recommended to repeat this study with a correct (orthonormal) implementation of the eigenfunctions to confirm the correctness of the presented results for all tidal divide heights.

A final important limitation is the used equilibrium tracking algorithm, which is not able to find the stable equilibrium in case unstable equilibria are located close to it. This occurs in particular close to boundaries where the system transitions from stable to unstable, hence the location of these boundaries is only indicative and cannot be determined with absolute certainty. However, analysis of the eigenvalues close to the boundaries has shown that

the tracking algorithm has come sufficiently close to the boundary. A new study with a more advanced and accurate equilibrium tracking algorithm is therefore recommended. In this study, an attempt was made to construct such a tracker based on a bifurcation analysis: finding all equilibria for a set of parameters which appropriately simplify the problem, after which the parameters can be stepwise adjusted to their desired values whilst tracking the known equilibria and checking for any bifurcations. Although this approach did not succeed, it seems a promising method to find equilibria more accurately and with more certainty that truly all existing equilibria are found. In Appendix D, some more details about this approach and the encountered complications are given.

7 Conclusion

This study has provided new information about tidal inlet stability in barrier coasts and the effect of small temporary perturbations on the inlets in a double and triple inlet system, as well as the effect of a tidal divide surrounding the middle inlet on the stability and connectivity of inlets. A process-based model based on the Escoffier (1940) principle that allows for a circular sector geometry was successfully implemented, allowing for the placement of a circular tidal divide circumventing the middle inlet whilst preserving the strengths of the solution method as introduced by Roos et al. (2013). Model results show that a barrier coast in this configuration can accommodate a stable equilibrium configuration with all three inlets open, even in absence of the tidal divide. When interpreting the results in terms of inlet connectivity, it has been shown that the size of the basin is negatively correlated with inlet connectivity: the larger the basin, the smaller the connectivity quotient. When applying this to the Western Wadden Sea system, it is concluded that this system can be in a stable configuration with all three inlets open and that the connectivity between all inlets is relatively low as a consequence of the large basin area.

The triple inlet system also allows for asymmetric connectivity, where the asymmetry in the inlet cross-sectional area has been shown to be decisive in the asymmetry in the connectivity quotient. Hence, it is concluded that the basin geometry and inlet location directly govern to what extent two inlets are connected. However, these parameters are only indirectly influencing the asymmetry in the inlet connectivity; these parameters directly lead to an asymmetry in the cross-sectional inlet area, which in turn leads to an asymmetry in inlet connectivity. Furthermore, the results show that the inclusion of a tidal divide does influence the connectivity between two inlets, but does not directly cause changes in connectivity asymmetry; these changes are only indirectly caused as the tidal divide changes the inlet areas, which correlates with the asymmetry in connectivity.

Additionally, the results have shown that the transition from a double to a triple inlet system allows for complicated dynamics in which positive connectivity quotients are sometimes encountered, although temporary positive

responses may be more common but overwhelmed by the negative responses. This behaviour seems impossible in a double inlet system but is allowed in a triple inlet system. Finally, all aforementioned results have been generated and explained in terms of two processes, being the bottom-friction and pressure-gradient in the tidal inlet (Roos et al., 2013). Combined with spatial water level variations in the basin, these processes introduce more complicated dynamics that capture the essential dynamics in barrier coast systems like the Western Wadden Sea.

References

Brouwer, R. L., Van de Kreeke, J., & Schuttelaars, H. M. (2012). Entrance/exit losses and cross-sectional stability of double inlet systems. *Estuarine, Coastal and Shelf Science*, *107*, 69–80. https://doi.org/10.1016/j.ecss.2012.04.033

Brouwer, R. L., Schuttelaars, H. M., & Roos, P. C. (2013). Modelling the influence of spatially varying hydrodynamics on the cross-sectional stability of double inlet systems. *Ocean Dynamics*, *63*(11-12), 1263–1278. https://doi.org/10.1007/s10236-013-0657-6

De Swart, H. E., & Zimmerman, J. T. F. (2009). Morphodynamics of tidal inlet systems. *Annual Review of Fluid Mechanics*, *41*, 203–229. https://doi.org/10.1146/annurev.fluid.010908.165159

Elias, E. P., Van Der Spek, A. J., Wang, Z. B., & De Ronde, J. (2012). Morphodynamic development and sediment budget of the Dutch Wadden Sea over the last century. *Netherlands Journal of Geosciences*, *91*(3), 293–310. https://doi.org/10.1017/S0016774600000457

Escoffier, F. F. (1940). The Stability of Tidal Inlets. *Shore and Beach*, *8*, 114–115.

Kragtwijk, N., Zitman, T., Stive, M., & Wang, Z. (2004). Morphological Response of Tidal Basins to Human Interventions. *Coastal Engineering*, *51*(3), 207–221.

Lorentz, H. A. (1922). Het in rekening brengen van den weerstand bij schommelende vloeistofbewegingen. *De Ingenieur*, *37*, 695.

Murray, A. B. (2003). Contrasting the goals, strategies, and predictions associated with simplified numerical models and detailed simulations. *Geophysical Monograph Series*, *135*, 151–165. https://doi.org/10.1029/135GM11

Reef, K. R. G., Roos, P. C., Schuttelaars, H. M., & Hulscher, S. J. M. H. (2020). Influence of Back-Barrier Basin Geometry on Multiple Tidal Inlet Systems: The Roles of Resonance and Bottom Friction. *Journal of Geophysical Research: Earth Surface*, *125*(3). https://doi.org/10.1029/2019JF005261

Roos, P. C., Schuttelaars, H. M., & Brouwer, R. L. (2013). Observations of barrier island length explained using an exploratory morphodynamic model. *Geophysical Research Letters*, *40*(16), 4338–4343. https://doi.org/10.1002/grl.50843

Salles, P., Voulgaris, G., & Aubrey, D. G. (2005). Contribution of nonlinear mechanisms in the persistence of multiple tidal inlet systems. *Estuarine, Coastal and Shelf Science*, *65*(3), 475–491. https://doi.org/10.1016/j.ecss.2005.06.018

Stive, M., Wang, Z., Capobianco, M., Ruol, P., & Buijsman, M. (1998). Morphodynamics of a Tidal Lagoon and the Adjacent Coast. *Physics of Estuaries and Coastal Seas, Eds. J. Dronkers and M.B.A.M. Scheffers*, 431.

UNESCO World Heritage Centre. (2009). Wadden Sea - UNESCO World Heritage Centre. https://whc.unesco.org/en/list/1314

van de Kreeke, J. (1990). Can multiple tidal inlets be stable? *Estuarine, Coastal and Shelf Science*, *30*(3), 261–273. https://doi.org/10.1016/0272-7714(90)90051-R

van de Kreeke, J., Brouwer, R. L., Zitman, T. J., & Schuttelaars, H. M. (2008). The effect of a topographic high on the morphological stability of a two-inlet bay system. *Coastal Engineering*, *55*(4), 319–332. https://doi.org/10.1016/j.coastaleng.2007.11.010

Zimmerman, J. T. (1976). Mixing and flushing of tidal embayments in the western Dutch Wadden Sea part I: Distribution of salinity and calculation of mixing time scales. *Netherlands Journal of Sea Research*, *10*(2), 149–191. https://doi.org/10.1016/0077-7579(76)90013-2

A Eigenfunction Derivation

Following Equation (16), the eigenfunctions for the closed basin water elevation should satisfy

$$\nabla \cdot \left(\frac{h_b}{\mu_b} \nabla \psi \right) + \frac{\omega^2}{g} \psi + \lambda \frac{h_b}{\mu_b} \psi = 0 \qquad \text{in } \Omega, \qquad (29)$$

with λ the eigenvalue and h_b/μ_b the (complex) weight function. For readability, subscripts m and n have been omitted. Furthermore, the problem satisfies the boundary conditions $\nabla \psi \cdot \mathbf{n} = 0$ on $d\Omega$, as well as $|\psi| < \infty$ if $r = 0$. At the locations of the discontinuities in the bottom elevation $R = R^a, R^b, ...$, we demand that continuity of water elevation and mass conservation, such that

$$\psi^L = \psi^R, \qquad \frac{h_b^L}{\mu_b^L} \frac{\partial \psi^L}{\partial r} = \frac{h_b^R}{\mu_b^R} \frac{\partial \psi^R}{\partial r} \qquad \text{at } r = R^{a,b}, \quad (30)$$

where superscripts L and R denote the left and right of the discontinuity location, respectively. Note that, within each compartment, the topography is uniform, such that Equation (29) can be rewritten to

$$\nabla^2 \psi + k_b^2 \mu_b \psi + \lambda \psi = 0, \qquad (31)$$

with $k_b^2 = \omega^2 h_b^{-1} g^{-1}$ the basin wave number.

The eigenfunction ψ is now easily solved by separation of variables, yielding

$$\psi = R(r) \Theta(\theta), \qquad (32)$$

where the solution for $\Theta(\theta)$ is well known and reading

$$\Theta(\theta) = D_m \cos\left(\frac{m\pi\theta}{\theta_b} \right) = D_m \cos\left(\nu_m \theta \right), \qquad (33)$$

with $\nu_m = m\pi/\theta_b$ the eigenvalue and D_m the normalisation coefficient, equating to $D_0^2 = \theta_b^{-1}$ and $D_m^2 = 2\theta_b^{-1}$ for $m = 1, 2, ...$ Substitution of Equation (32) in Equation (29), combined with the aforementioned definition of $\Theta(\theta)$, then yields the differential problem for $R(r)$, reading

$$r^2 \frac{d^2 R}{dr^2} + r \frac{dR}{dr} + \left[\beta^2 r^2 - \nu_m^2 \right] R = 0, \quad \beta^2 = \mu_b k_b^2 + \lambda, \quad (34)$$

where we explicitly note that β is allowed to be complex as μ_b is a complex number (Roos & Schuttelaars, to be published). This equation takes the shape of Bessel's differential equation of order ν_m, such that the solutions for R are to be sought in the Bessel functions. It is indeed easily verified that

$$R(r) = C_1 J_{\nu_m}(\beta r) + C_2 Z_{\nu_m}(\beta r), \qquad (35)$$

where

$$Z_a(\beta r) = \begin{cases} Y_a(\beta r) & \text{if } \nu_m = 0, 1, 2, ... \\ J_{-a}(\beta r) & \text{otherwise,} \end{cases} \qquad (36)$$

solve our differential equation. We note here, however, that the value for β is depending on the compartment of the basin, as well as the coefficients C_1 and C_2, which we still need to solve for.

Solving these is achieved by reviewing the continuity conditions at the interfaces and substituting the equation found for ψ. Evaluating both constraints then yields

$$C_1^L J_i^L + C_2^L Z_i^L = C_1^R J_i^R + C_2^R Z_i^R,$$

$$\frac{h_b^L \beta^L}{\mu_b^L} \left[C_1^L J_i^{L\prime} + C_2^L Z_i^{L\prime} \right] = \frac{h_b^R \beta^R}{\mu_b^R} \left[C_1^R J_i^{R\prime} + C_2^R Z_i^{R\prime} \right],$$

where we introduced the shorthand notation $J_i^{L,R} = J_{\nu_m}(\beta^{L,R} R_i)$ and similarly for Z; furthermore, primes are used to denote derivatives with respect to r. Superscripts denote the radial compartment of the basin, with L and R denoting either side of the topographic step, explicitly showing the dependence of β and the coefficients C on the basin compartment. In our implementation, the recurrence relations for Bessel functions have been used to reformulate the derivative terms. Additionally, the boundary conditions are applied as additional constraints to the constants C_1 and C_2, which are written into a linear system of equations. For a system with two discontinuities (at R^a and R^b), separating the basin in three compartments (denoted with superscripts a, b, c from origin to R_b), we then obtain $\mathbf{Mc} = \mathbf{0}$, where

$$\mathbf{M} = \begin{bmatrix} J_1^a & -J_1^b & -Z_1^b & 0 & 0 \\ \xi^a J_1^{a\prime} & -\xi^b J_1^{b\prime} & -\xi^b Z_1^{b\prime} & 0 & 0 \\ 0 & J_2^b & Z_2^b & -J_2^c & -Z_2^c \\ 0 & \xi^b J_2^{b\prime} & \xi^b Z_2^{b\prime} & -\xi^c J_2^{c\prime} & -\xi^c Z_2^{c\prime} \\ 0 & 0 & 0 & J_b^{c\prime} & Z_b^{c\prime} \end{bmatrix},$$

$$\mathbf{c} = (C_1^a, C_1^b, C_2^b, C_1^c, C_2^c)^\top \qquad (37)$$

where the condition $C_2^a = 0$ has already been applied and $\xi = h_b/\mu_b$ for a specific compartment. As we demand a non-trivial solution to exist, we are interested in a solution for which the aforementioned system yields non-zero constants, requiring that $\det(\mathbf{M}) = 0$.

With this constraint, the values for β can be solved, as these are all a function of the unknown λ. The determinant of matrix $\mathbf{M}$ is numerically minimised (visualised in Figure 13) by tracing the branches in the complex plane of β^a where $\Im(\det(\mathbf{M})) = 0$ (red lines), after which the branch is followed until finding a point where $\Re(\det(\mathbf{M})) = 0$ (blue lines). At this point, a local minimisation algorithm is applied to further reduce $|\det(\mathbf{M})|$. After finding λ, the constants can be solved based on Equation (37), where we additionally demand that $C_1^a = 1$ to come to a solvable system. This is afterwards corrected by demanding orthonormality of the eigenfunctions, i.e. demanding that

$$\int_0^{R_b} \frac{h_b}{\mu_b} r R^2(r) dr = 1, \qquad (38)$$

which is practically implemented by numerically computing this integral for known constants $\mathbf{c}$, and dividing all constants by the result of this integral.
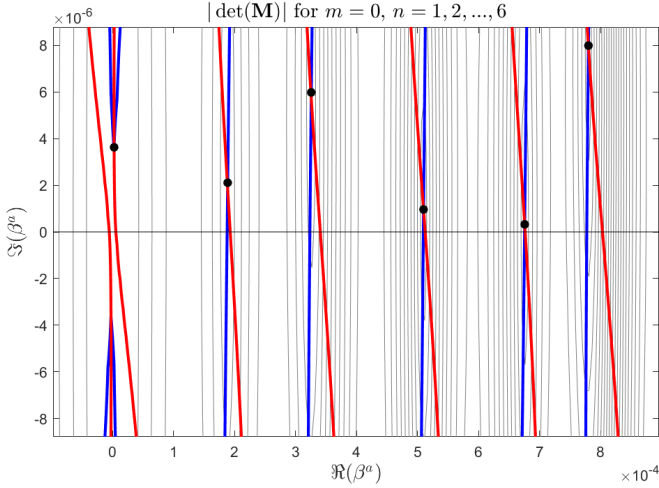
Figure 13: Visualisation of the $|\det(\mathbf{M})|$ as a function of the real and imaginary part of β^a. Blue lines are isolines where $\Re(\det(\mathbf{M})) = 0$, red where $\Im(\det(\mathbf{M})) = 0$.

B Width-Averaging over Inlet Mouth

Width-averaging the eigenfunctions over the inlet mouth is required to find the expressions for the basin-impedances. In this procedure, it is assumed that the inlet is not facing a topographic step in the basin. As such, the width average of the inlet can be formulated as

$$\langle \psi \rangle_j = \frac{1}{b_j} \int_{R_j - \frac{b_j}{2}}^{R_j + \frac{b_j}{2}} \psi(\theta_j, r) dr. \quad (39)$$

However, as there are different formulations for eigenfunctions (depending whether or not ν_m is an integer), also different expressions for the integrals. The aim is to reduce all integrals to a direct expression or an infinite summation series, allowing for accurate inclusion in Matlab. An additional constraint to these equations is that they should not become infinite summation series where the terms are not converging to zero in a sufficiently fast pace. This because the Matlab implementation of such series becomes inaccurate.

B.1 Averaging BesselJ-functions

Integrating J_{ν_m} over the inlet mouth can be relatively directly be done using the expression

$$\int J_a(br) dr = \frac{2}{b} \sum_{k=0}^{\infty} J_{a+2k+1}(br), \quad (40)$$

which holds for all values of a. This is easily applied for the first term of ψ, as well as to Z if ν_m is integer.

B.2 Averaging BesselY-function

Averaging Y_{ν_m} over the inlet mouth is a little more involved, as two different expressions exist for cases with ν_m being even or odd. In case ν_m is odd, the integration

rule

$$\int Y_{\nu_m}(br) dr = -\frac{1}{b} Y_0(br) - \frac{2}{b} \sum_{k=0}^{\nu_m/2 - 1/2} Y_{2k}(br) \quad (41)$$

can be applied. The situation is a little more involved for even ν_m, for which we can use the integration rule

$$\int Y_{\nu_m}(br) dr = -\frac{2}{b} \sum_{k=1}^{\nu_m/2} Y_{2k+1}(br)$$
$$+ \frac{\pi}{2} r \left[Y_0(br) H_{-1}(br) + Y_1(br) H_0(br) \right], \quad (42)$$

where H denotes the Struve function. To avoid inefficient converging behaviour, we avoid the power series and instead express H in terms of of Bessel functions. For this, we rewrite the recurrence relation for the Struve function to find

$$H_{-1}(x) = -H_1(x) + \frac{1}{\sqrt{\pi}\Gamma\left(\frac{3}{2}\right)}, \quad (43)$$

after which the expansions

$$H_0(z) = \frac{4}{\pi} \sum_{k=0}^{\infty} \frac{J_{2k+1}(z)}{2k+1}, \quad (44)$$

$$H_1(z) = \frac{2}{\pi} (1 - J_0(z)) + \frac{4}{\pi} \sum_{k=1}^{\infty} \frac{J_{2k}(z)}{4k^2 - 1}, \quad (45)$$

complete the integral formulation.

B.3 Averaging over the Origin

In the case that $\theta_b = \pi$, we wish to allow the inlets to stretch over the origin, enabling the simulation of a perfectly symmetric system. For this case, we need to split the integral over the two parts of the boundary, yielding

$$\langle \psi \rangle_j = \int_{R_j - \frac{b_j}{2}}^{0} \psi(|\theta_j - \theta_b|, r) dr + \int_{0}^{R_j + \frac{b_j}{2}} \psi(\theta_j, r) dr, \quad (46)$$

where the integrals can be computed by the aforementioned expressions. Here, we do note that, in the first compartment, $C_2^a = 0$, limiting the eigenfunction to the J_{ν_m}-term.

B.4 Exception $\beta = 0$

An important exception is to be included for $m = 0$, $n = 1$ where the value of β will equate to zero in the outer part of the domain (and possibly other parts with the same water depth). For all inlets located in these parts of the domain, the average equals to

$$\langle \psi \rangle_j = \sqrt{2} R_b^2 \theta_b h_b^j, \quad (47)$$

with h_b^j the water depth of the compartment of the domain that inlet j faces.

C   Analytical Jacobi Matrix

For analysis of the stability of the equilibria, an expression for the Jacobi matrix is required which, with some writing, is relatively easily found analytically. For convenience, we write $\mathbf{f} = d\mathbf{A}/dt$, after which taking the derivative of the Escoffier equation (Eqn. (3)) with respect to A_j yields

$$\frac{\partial f_i}{\partial A_j} = \frac{3 M_{\text{sed}}}{l U_{eq}^3} |\hat{u}_i|^2 \frac{\partial |\hat{u}_i|}{\partial A_j}$$
$$= \frac{3 M_{\text{sed}}}{2 l U_{eq}^3} |\hat{u}_i| \left[\hat{u}_i \frac{\partial \hat{u}_i^*}{\partial A_j} + \hat{u}_i^* \frac{\partial \hat{u}_i}{\partial A_j} \right], \qquad (48)$$

where * denotes taking the complex conjugate, and where we note that $d\hat{u}^*/dA = (d\hat{u}/dA)^*$. Recall that the Equation (15) were written as $\mathbf{N}\hat{\mathbf{u}} = \mathbf{F}$ where $\mathbf{F} \neq \mathbf{F}(\mathbf{A})$, such that taking the derivative with respect to A_j at both sides yields

$$\frac{\partial}{\partial A_j} [\mathbf{N}\hat{\mathbf{u}}] = 0, \text{ such that } \frac{\partial \hat{\mathbf{u}}}{\partial A_j} = -\mathbf{N}^{-1} \frac{\partial \mathbf{N}}{\partial A_j} \hat{\mathbf{u}}. \qquad (49)$$

Taking the derivatives of the matrix $\mathbf{N}$ is also relatively easily done, although one needs to distinguish three different cases, yielding

$$\frac{\partial \mathbf{N}_{pq}}{\partial A_j} = \begin{cases} \frac{\omega \mathrm{i}}{g} \sum_{m,n} \frac{\langle \psi \rangle_q A_q}{\lambda} \frac{\partial \langle \psi \rangle_p}{\partial A_j} & p = j, q \neq j, \\ \frac{\omega \mathrm{i}}{g} \sum_{m,n} \frac{\langle \psi \rangle_p}{\lambda} \left[\langle \psi \rangle_q + \frac{\partial \langle \psi \rangle_q}{\partial A_j} A_q \right] & p \neq j, q = j, \\ \frac{\omega \mathrm{i}}{g} \sum_{m,n} \left[\frac{\langle \psi \rangle_p}{\lambda} \left[\langle \psi \rangle_q + 2 A_q \frac{\partial \langle \psi \rangle_q}{\partial A_j} \right] \right] + \frac{\mathrm{i}\omega l_j}{g} \frac{\partial \mu_j}{\partial A_j} & p = q = j, \\ 0 & \text{otherwise.} \end{cases} \qquad (50)$$

It is easily computed that

$$\frac{\partial \mu_j}{\partial A_j} = -\frac{r_j}{2\mathrm{i}\omega \gamma_j} A_j^{-\frac{3}{2}}. \qquad (51)$$

The derivatives of the width-averaged eigenfunctions are easily found by applying Leibniz' integration rule to find

$$\frac{\partial \langle \psi \rangle_j}{\partial A_j} = -\frac{1}{2 A_j} \langle \psi \rangle_j + \frac{1}{4 A_j} \left[\psi \left(R_j^+ \right) + \psi \left(R_j^- \right) \right], \qquad (52)$$

with $R_j^\pm = R_j \pm b_j/2$, completing the analytical expression for the Jacobi matrix. It should be appreciated that this expression is not depending on the form of ψ, yielding a general result that may also be applied to other geometries.

D   Bifurcation Analysis

For reliably tracking all the present equilibria in a 3D vector-field, the use of a bifurcation analysis seems a feasible option. In this study, the implementation of such a tracker was not successful, but this appendix should give some more details and thoughts about this, hopefully contributing to a successful implementation in the future.

The idea behind the use of a bifurcation analysis as equilibrium tracking tool is to choose an independent bifurcation parameter (for instance the basin water depth) which is systematically varied. This parameter should satisfy two important conditions: 1) in the default situation, one should be able to analytically compute the equilibria, or to numerically compute them and proof that all equilibria are found; 2) during the systematic parameter variation, all new equilibria should emerge from existing equilibria, and no new branches should come to existence. If these two conditions are met, the use of a bifurcation analysis as equilibrium tracking algorithm seems promising, as it would allow for relatively cheap and reliable tracking of all equilibria without having to compute the full vector field first. Furthermore, such a tracking algorithm can reliably locate equilibria that are located close to one another, whilst the algorithm from this study has large difficulty with such situations.

In the process to develop such an algorithm, two main difficulties were encountered, the first being the choice of an appropriate bifurcation parameter. This because the two conditions posed are essentially contradicting: condition 1) demands the system to be as simple as possible, whilst condition 2) demands that sufficient equilibria are already present in the system. Furthermore, in case a tidal divide is present in the system, bifurcation parameter is preferred such that the eigenfunctions are independent of the parameter. This because it is impossible to find analytical derivatives for the eigenvalues with respect to the independent parameters; hence, one should resort to numerical computation, which is undesirable as algorithm for tracking the eigenvalues is computationally demanding in itself. One could also think of introducing a special bifurcation parameter, for instance by splitting the impedance matrix in Equation 15 in two parts; $\tilde{\mathbf{Z}}$, containing the inlet friction and the first mode of the basin impedances Z_{jq} $(m = 0, n = 1)$; and $\bar{\mathbf{Z}}$, containing all the remaining modes. One could then introduce a bifurcation parameter p which is varied from 0 to 1 and write

$$(\tilde{\mathbf{Z}} + p\bar{\mathbf{Z}})\hat{\mathbf{u}} = \hat{\eta}. \qquad (53)$$

Obviously, many more different choices could be made.

The second difficulty arising was in building a robust algorithm for the numerical continuation, as the matrices from the continuation algorithm turned out to be singular too often for successful implementation. A particular problem is that a triple inlet system is mathematically

not in equilibrium if one inlet is closed, as a consequence of the assumption that sediment import M_{sed} is independent of the inlet size, also in case that inlet is closed. As a consequence of this, the matrix becomes singular when imposing an inlet area to equate to zero, complicating the analysis. A solution could be to adapt the equations such that the derivative $\partial A_i/\partial t = 0$ if $A_i = 0$.

The reward, however, in case one manages to successfully implement such an algorithm may be vast. After all, this analysis method is easily extended for multi-dimensional systems (more than three inlets) with a relatively low increase in computational demand. Furthermore, one should be able to proof that one found all equilibria in the system by using some symmetry-properties of the impedance matrix in Equation 15. After all, when writing the equation (but now for a double inlet system) as

$$\begin{bmatrix} \frac{\mathrm{i}\omega l}{g}\mu_1 + Z_{11} & Z_{12} \\ Z_{21} & \frac{\mathrm{i}\omega l}{g}\mu_2 + Z_{22} \end{bmatrix} \begin{pmatrix} A_1\hat{u}_1 \\ A_2\hat{u}_2 \end{pmatrix} = \begin{pmatrix} \hat{\eta}_{o1} \\ \hat{\eta}_{o2} \end{pmatrix}, \quad (54)$$

the matrix on the left-hand-side has become symmetric due to the symmetric definition of the basin impedances (see Eqn. 21). If one chooses the bifurcation parameter appropriately, one may even be able to make this matrix consisting of imaginary numbers only, and the (combination of) these properties can potentially be exploited to show that all equilibria are found.

Based on these considerations, it can be concluded that the use of a bifurcation analysis as method to track the equilibria can be a reliable and cheap solution to find the equilibria, also allowing for easy extension to systems with more than three inlets. Although this study did not succeed in developing such an algorithm, it is hoped that the insights from this appendix can contribute to the implementation eventually.